

On signatures of clouds in exoplanetary transit spectra

Arazi Pinhas[★] and Nikku Madhusudhan[★]

Institute of Astronomy, University of Cambridge, Madingley Road, Cambridge CB3 0HA, UK

Accepted 2017 July 19. Received 2017 June 29; in original form 2017 February 23

ABSTRACT

Transmission spectra of exoplanetary atmospheres have been used to infer the presence of clouds/hazes. Such inferences are typically based on spectral slopes in the optical deviant from gaseous Rayleigh scattering or low-amplitude spectral features in the infrared. We investigate three observable metrics that could allow constraints on cloud properties from transmission spectra, namely the optical slope, the uniformity of this slope and condensate features in the infrared. We derive these metrics using model transmission spectra considering Mie extinction from a wide range of condensate species, particle sizes and scaleheights. First, we investigate possible degeneracies among the cloud properties for an observed slope. We find, for example, that spectra with very steep optical slopes suggest sulphide clouds (e.g. MnS, ZnS, Na₂S) in the atmospheres. Secondly, (non)uniformities in optical slopes provide additional constraints on cloud properties, e.g. MnS, ZnS, TiO₂ and Fe₂O₃ have significantly non-uniform slopes. Thirdly, infrared spectra provide an additional powerful probe into cloud properties, with SiO₂, Fe₂O₃, Mg₂SiO₄ and MgSiO₃ bearing strong infrared features observable with *James Webb Space Telescope*. We investigate observed spectra of eight hot Jupiters and discuss their implications. In particular, no single or composite condensate species considered here conforms to the steep and non-uniform optical slope observed for HD 189733b. Our work highlights the importance of the three above metrics to investigate cloud properties in exoplanetary atmospheres using high-precision transmission spectra and detailed cloud models. We make our Mie scattering data for condensates publicly available to the community.

Key words: radiative transfer – scattering – planets and satellites: atmospheres – planets and satellites: composition – planetary systems.

1 INTRODUCTION

Transmission spectroscopy has been one of the most successful methods in characterizing exoplanetary atmospheres (see e.g. Burrows 2014; Madhusudhan et al. 2016). Studies of planets in transit have been used to infer a wide variety of properties such as clouds and hazes, molecular abundances and pressure–temperature structures (Demory et al. 2013; Pont et al. 2013; Knutson et al. 2014a,b; Kreidberg et al. 2014a,b; Madhusudhan et al. 2014; Sing et al. 2016). One of the major inferences from optical and near-infrared (NIR) transmission spectroscopy in recent years is the incidence of clouds and hazes in exoplanetary atmospheres. The terms ‘clouds’ and ‘hazes’, collectively regarded as ‘aerosols’, are used in different contexts in the literature. From a formation standpoint, ‘haze’ implies particles formed through photochemical processes whereas a ‘cloud’ constitutes particles formed through condensation of vapour on to a nucleus under suitable thermodynamic conditions (Marley

et al. 2013). On the other hand, these terms are also used in reference to the spectral features they can cause, especially in parametric models used for atmospheric retrieval or otherwise (e.g. Benneke & Seager 2012; Kreidberg et al. 2014b; Sing et al. 2016; MacDonald & Madhusudhan 2017). A ‘cloud’ is generally used to mean a source of grey opacity and high optical depth effective below some height in the atmosphere, while a ‘haze’ is represented by an opacity in the optical through a power-law dependence on wavelength (see e.g. MacDonald & Madhusudhan 2017). Our work is more closely associated with clouds defined through the formation standpoint, and we therefore use this terminology throughout our work.

Two basic avenues are used to infer the dominant role of clouds in exoplanetary atmospheres. First, observations of transmission spectra with slopes in the optical that deviate from the canonical Rayleigh slope of -4 are attributed to the presence of clouds and hazes (Pont et al. 2013; Sing et al. 2016). Secondly, nearly flat spectra in the NIR have also suggested the dominance of clouds, especially for Neptune analogues and super-Earths (Knutson et al. 2014a,b; Kreidberg et al. 2014a).

Cloud inferences are now widely prevalent. For example, Sing et al. (2016) observed the atmospheres of 10 hot Jupiters and

[★] E-mail: ap817@cam.ac.uk, ap817@ast.cam.ac.uk (AP); nmadhu@ast.cam.ac.uk (NM)

interpreted these as ranging from cloudy to clear. Clouds have also been inferred on rocky exoplanets through transmission spectroscopy. The super-Earth, GJ 1214b, has a transit spectrum devoid of absorption features with clouds as the leading explanation (Kreidberg et al. 2014a). Howe & Burrows (2012)'s ad hoc haze can fit the observations and Morley et al. (2013) have suggested that KCl and ZnS clouds with large scaleheights may cause the flat spectrum if the atmospheric composition is supersolar in metallicity. Mbarek & Kempton (2016) have recently extended the putative condensate species responsible for the spectrum of GJ 1214b, raising the possibility of potassium sulphate (K_2SO_4), zinc oxide (ZnO) and/or graphite clouds. Whilst the strongest interpretation of GJ 1214b's spectrum is clouds, the other possibility is a relatively small atmospheric extent due to a high mean molar mass of atmospheric gas (Bean et al. 2011). Similar inferences of clouds have been attributed to several other transiting exoplanets with flat spectra such as HD 97658b (Knutson et al. 2014b), exo-Neptune GJ 436b (Knutson et al. 2014a) and exo-Uranus GJ 3470b (Ehrenreich et al. 2014).

Hot Jupiters have been studied in transit more extensively than super-Earths and Neptunian analogues due to more pronounced atmospheric signatures. The transit spectrum of HD 189733b in the optical to NIR bears a steep slope that almost completely obscures Na and K alkali signatures (Pont et al. 2013); this slope is hypothesized to be due to small (i.e. $\sim 10^{-2}$ μm) particulates characterized by efficient isotropic scattering of photons (Lecavelier Des Etangs et al. 2008; Pont et al. 2008; Lee et al. 2014; Wakeford & Sing 2015). Lecavelier Des Etangs et al. (2008) suggest HD 189733b's steep slope to be due to $MgSiO_3$ (enstatite) particulates. Wakeford & Sing (2015) predict clouds dominated by particles of size 0.025 μm , though their condensate models are statistically poor fits to observations especially for wavelengths below 0.5 μm . Lee et al. (2016) have recently suggested that the transit spectrum of HD 189733b may be sampling a combination of cloud compositions.

Fortney (2005) highlights the greater influence clouds have in transit than for normal viewing angle at secondary eclipse. The longer path-length offered in transit implies more extinction by cloud particles and conveys their importance in models to be able to relate to transmission observations. To this end, many cloud models have been formulated of which some have been used to understand transit spectra. Ackerman & Marley (2001) present a cloud model for substellar atmospheres that incorporates a balance between upward turbulent diffusion and downward sedimentation. Detailed non-equilibrium dust modelling that includes nucleation, heterogeneous growth, gravitational settling and subsequent evaporation and efficient convection of the evaporated particulates is considered by Helling (2008) and Helling et al. (2008). Helling et al. (2016) have used the latter models to investigate cloud physics in HD 209458b and HD 189733b with three-dimensional atmospheric simulations. Wakeford & Sing (2015) have used the analytic model of Lecavelier Des Etangs et al. (2008) to explore the transmission spectra of clouds in hot Jupiters. Wakeford et al. (2017) followed on this with a study of cloud condensates in superhot Jupiters, with a focus on cloud formation in WASP-12b. Using a minimal χ^2 statistical fit, they determine particle sizes of corundum (Al_2O_3) and perovskite ($CaTiO_3$) in the atmosphere of WASP-12b to be 0.001–0.25 and 0.025–0.1 μm , respectively. Line & Parmentier (2016) recently investigated the role of inhomogeneous or patchy clouds on transmission spectra of exoplanets. Heng (2016) associated the sodium and potassium line properties in the optical with the degree of cloudiness in atmospheres of transiting exoplanets. Cloud studies and cloud models such as these and others have been used to explore the diversity of clouds in exoplanetary atmospheres (Marley et al. 2013).

Our goal in the present work is to investigate in detail observable cloud spectral features of importance for interpretation of high-precision transit spectra. There are in principle three key observable components to study clouds using transmission spectra: the slope of a spectrum in the optical, the uniformity of this slope and extinction features in the infrared (IR). Whilst gaseous Rayleigh scattering leads to a slope of -4 , we show that condensates can lead to slopes over a broad range from -13 to 1 . We study in detail the degeneracies in observed optical slopes that arise from a combination of condensate species, modal particle sizes and cloud scaleheights. We also explore the extent to which these slopes are uniform and thereby their potential to reduce degeneracies in inferring cloud properties. These two observables promise to be powerful means of understanding clouds in the optical, especially with future high-precision observations. We also study condensate signatures in the IR and show four species to have strong features. This third observable is of great promise due to the imminent launch of *James Webb Space Telescope (JWST)*. The plethora of current and forthcoming observations in the optical and IR domains from *Hubble Space Telescope (HST)*, *Spitzer*, *Very Large Telescope (VLT)*, *JWST* and forthcoming Extremely Large Telescopes (ELTs; e.g. E-ELT, GMT and TMT) motivate our present study.

The paper is organized as follows. Our numerical transmission model for clouds is developed in Section 2, along with the Mie theory of light interactions with spherical microparticles. We then use these Mie opacities in Section 3 to address the three key observables discussed above and illustrate their importance for future high-precision observations. In Section 4, we discuss applications to hot Jupiters HD 189733b and HD 209458b, which have some of the highest precision observations. We then discuss model limitations and conclude our work with a review of the essential outcomes of our study in Section 5.

2 METHODS

We here develop a model for the transmission spectrum of a cloudy atmosphere. Section 2.1 discusses our numerical transmission model and the slant optical depth of the transit geometry. We then introduce our Mie theory code for a single cloud particle size in Section 2.2. We generalize our cloud opacity to include particle size distributions in Section 2.4. Section 2.5 then summarizes the model parameters.

2.1 Transmission model

We develop a model for the transmission spectrum of a cloudy atmosphere by considering the transit depth. The transit depth is the measured fractional diminution in the stellar light at a given wavelength when the planet transits its host star. Through considering how much flux is absorbed in the planetary atmosphere, we can derive the transit depth as (see Appendix A)

$$\Delta(\lambda) = \left(\frac{R_{p,\lambda}}{R_*} \right)^2 = \frac{2}{R_*^2} \int_0^\infty r(1 - e^{-\tau(\lambda,r)})dr. \quad (1)$$

Here $\tau(\lambda, r)$ is the slant optical depth along the line of sight at a radius r from the planetary centre. The transit depth is the sum of each planetary annulus $2\pi r dr$ weighted by its corresponding absorbance $1 - e^{-\tau(\lambda,r)}$, relative to the projected area of the stellar disc. This can be solved exactly numerically. In the present work, we assume a simplified numerical model to computing the transit depth. We herein describe our model and its assumptions.

To begin with we consider a simplified approach wherein an effective altitude is used to represent the whole atmosphere. Lecavelier Des Etangs et al. (2008) calculated a planet-independent effective slant optical depth for a range of R_{p0}/H (R_{p0} is a fiducial planetary radius at a certain λ and H is the atmospheric scaleheight) such that the translucent atmosphere of a planet produces an equivalent effect as a sharp occulting disc. The sharp occulting disc model has a transit depth of

$$\Delta(\lambda) = \left(\frac{R_{p,\lambda}}{R_*} \right)^2 = \left(\frac{R_{p0} + z_{\text{eff}}(\lambda)}{R_*} \right)^2. \quad (2)$$

The slant optical depth at the top of the occulting disc is $\tau_{\text{eff}} = 0.56$ and defines the effective altitude z_{eff} at a given λ . We have carried out a numerical comparison of the exact formulation in equation (1) with the fiducial numerical model in equation (2) and find they differ only by ~ 1 per cent. In our model, the reference pressure p_0 associated with R_{p0} is a free parameter and depending on its value, $z_{\text{eff}}(\lambda)$ can lie either below or above R_{p0} .

The transit depth Δ or its proxy z_{eff}/H computed through our numerical scheme is consistent with that obtained using the formulation of Lecavelier Des Etangs et al. (2008). Both our formulations consider R_{p0} as a reference level that can vary in the atmosphere through p_0 . A comparison with a formulation that regards R_{p0} as a hard surface is discussed in Appendix A. In our model, we start our calculation of the slant optical depth τ from the bottom of an isothermal atmosphere determined by the equilibrium temperature T_{eq} at a base pressure of $p_{\text{base}} = 10$ bar. We work differentially upwards assuming spherical symmetry until the effective slant optical depth of $\tau_{\text{eff}} = 0.56$ is reached.

We use a numerical scheme in our work to calculate z_{eff}/H as described in Section 2.1.1 because the z_{eff}/H of Lecavelier Des Etangs et al. (2008) cannot be calculated analytically for atmospheres with clouds of scaleheights different from the gas scaleheight and with multiple opacity sources (e.g. clouds, H_2 Rayleigh scattering, etc.). Nevertheless, the peculiar combination of clouds and H_2 scattering produces slopes that are nearly equivalent to a pure cloud opacity for cloud scaleheights larger than $H_c \approx 2H/5$ (the differences being about $\lesssim 1$ per cent). Therefore, the analytical formalism of Lecavelier Des Etangs et al. (2008) for this combination is valid upwards of $H_c \approx 2H/5$. Within the interval $H_c \approx 2H/5$ to $H_c = H$, the instantaneous slope of the effective altitude at any wavelength is then

$$\frac{d(z_{\text{eff}}/H)}{d \ln \lambda} \approx \gamma \frac{H_c}{H} \equiv \gamma \aleph_1, \quad (3)$$

where γ is the power on the effective extinction cross-section, $\sigma' = \sigma_0(a)(\lambda/\lambda_0)^{\gamma(a,\lambda)}$ with a the particle size and \aleph_1 is the ratio of the cloud scaleheight to the bulk atmospheric scale height.

2.1.1 Slant optical depth

Our numerical model considers various sources of opacity. These are absorption and scattering by cloud condensates, H_2 Rayleigh scattering and absorption by volatile gas species. We consider the latter gas component to include three contributions: H_2O , collision-induced absorption (CIA) $\text{H}_2\text{--H}_2$ and CIA $\text{H}_2\text{--He}$. The important radiative microphysics is contained in the slant optical depth $\tau(\lambda, y)$, where y is the vertical distance from the base pressure level of the atmosphere p_{base} . By considering the line-of-sight transit geometry, it is possible to derive that the optical depth along the line of sight

(Fortney 2005) for a cloudy H_2 -rich atmosphere is

$$\begin{aligned} \tau(\lambda, y) &= \tau_c(\lambda, y) + \tau_{\text{H}_2}(\lambda, y) + \tau_{\text{gas}}(\lambda, y) \\ &\approx \sigma'_c(a, \lambda) n_{\text{tot,b}} \xi_{\text{grain}} e^{-y/H_c} \sqrt{2\pi R_{p0} H_c} \\ &\quad + \sigma_{\text{H}_2}(\lambda) n_{\text{tot,b}} \xi_{\text{H}_2} e^{-y/H} \sqrt{2\pi R_{p0} H} \\ &\quad + \sigma_{\text{H}_2\text{O}}(\lambda) n_{\text{tot,b}} \xi_{\text{H}_2\text{O}} e^{-y/H} \sqrt{2\pi R_{p0} H} \\ &\quad + \sigma_{\text{H}_2\text{--H}_2}(\lambda) (n_{\text{tot,b}} \xi_{\text{H}_2})^2 e^{-y/H} \sqrt{2\pi R_{p0} H} \\ &\quad + \sigma_{\text{H}_2\text{--He}}(\lambda) (n_{\text{tot,b}})^2 \xi_{\text{H}_2} \xi_{\text{He}} e^{-y/H} \sqrt{2\pi R_{p0} H}, \end{aligned} \quad (4)$$

where $\sigma_{\text{H}_2}(\lambda)$ is (Seager 2010)

$$\sigma_{\text{H}_2}(\lambda) = \frac{8.14 \times 10^{-57}}{\lambda^4} + \frac{1.28 \times 10^{-70}}{\lambda^6} + \frac{1.61 \times 10^{-84}}{\lambda^8} \text{ [m}^2\text{]}. \quad (5)$$

Here, $\sigma'_c(a, \lambda)$ is the total effective cross-section of the cloud or condensate species; $n_{\text{tot,b}}$, the total atmospheric number density at the base pressure; ξ_i , the mixing ratio of a given opacity species; and H_c is the condensate scaleheight where we have assumed $n_c(r) = n_{c,b} e^{-y/H_c}$. Finally, we obtain the effective altitude z_{eff} through

$$z_{\text{eff}} = y_{\text{eff}} - H \ln \frac{p_{\text{base}}}{p_0}. \quad (6)$$

The effective altitude is calculated by determining the height y where a $\tau_{\text{eff}} = 0.56$ is reached, and subtracting from this the distance between the base location at p_{base} and the reference radius R_{p0} at p_0 .

2.2 Mie extinction from single cloud particles

It is necessary to use a physical theory for the absorption and scattering of light by microparticles to explore the varied effects of condensates on transmission spectra. Mie theory is such a theory; it is a solution of Maxwell's equations that considers interactions of electromagnetic radiation with spherical particles. When a solid or liquid particle is illuminated by an electromagnetic wave, electric charges in the particle transform into dipolar antennas that re-radiate waves producing 'scattered' radiation. The excited elementary charges may also transform a portion of the incident energy into thermal energy in a process of absorption.

The efficiencies of scattering and absorption as a function of wavelength are quantified by components of a complex index of refraction, $m(\lambda) = n(\lambda) + i\kappa(\lambda)$. The real index of refraction, $n(\lambda)$, informs about scattering whilst the imaginary index, $\kappa(\lambda)$, describes attenuation through absorption. We use the refractive index data from Wakeford & Sing (2015) for condensate species that are expected to condense in hot Jupiter atmospheres and that have experimental data in the optical and IR: Na_2S , MnS , ZnS , MgSiO_3 , SiO_2 , Al_2O_3 , FeO , Fe_2O_3 , TiO_2 , NaCl , KCl and Fe-rich Mg_2SiO_4 . There are therefore 12 condensate species with 12 elemental compositions represented in our work. We do not consider the effect of rainout of species. In principle, an element in one type of cloud species can limit the formation of other cloud species at higher altitudes due to the depletion of that element. Mbarek & Kempton (2016) discuss the effects of rainout on cloud type formation. For example, without including rainout, Fe and FeS clouds may both form in an atmosphere. An account of rainout suggests that the availability of Fe undergoes significant depletion so that FeS does not tend to form above the deeper Fe clouds, with S associating with Na rather than Fe to form Na_2S condensates at higher altitudes. This can then deplete Na that limits the condensation of NaCl clouds higher in the atmosphere, instead favouring KCl condensation.

We implemented our own Mie theory code in PYTHON that is similar to the classical code of Bohren & Huffman (1983). We make our condensate data calculated with our code publicly available to the community.¹ We briefly describe the formulation here. For a spherical particle of radius a embedded in radiation of wavelength λ , we can define a dimensionless size parameter x ,

$$x \equiv \frac{2\pi a}{\lambda}, \quad \text{where} \quad (7)$$

$$\lambda = \frac{\lambda_0}{m_s}. \quad (8)$$

Here, λ_0 is the wavelength of the incident light in vacuum and m_s is the real refractive index of the ambient medium surrounding the particle. The complex refractive index, $m(\lambda)$, for a particle of specific composition can be used to generate scattering and total extinction cross-sections (Deirmendjian 1969),

$$\sigma_{\text{scat}} = (\pi a^2) \frac{2}{x^2} \sum_{n=1}^{\infty} (2n+1) \{|a_n(m, x)|^2 + |b_n(m, x)|^2\}, \quad (9)$$

$$\sigma_{\text{ext}} = (\pi a^2) \frac{2}{x^2} \sum_{n=1}^{\infty} (2n+1) \text{Re}\{a_n(m, x) + b_n(m, x)\}, \quad (10)$$

where a_n and b_n are coefficients expressed in terms of Bessel functions of the first kind with fractional orders $\zeta = n \pm 1/2$. The absorption coefficient follows from the relation $\sigma_{\text{ext}} = \sigma_{\text{abs}} + \sigma_{\text{scat}}$. There are multiple ways to express the coefficients a_n and b_n , with the most popular in Bohren & Huffman (1983, see page 127) and Deirmendjian (1969, see page 17). Appendix B discusses the details of computing these coefficients in more detail. The number of terms needed for computations in the sum for the scattering and extinction cross-sections scales monotonically with the value of the size parameter, and the maximum number of terms needed for good convergence is given by $n_{\text{max}} = \max\{x + 4x^{1/3} + 2, |mx|\} + 15$ (Bohren & Huffman 1983).

We use the above formalism to generate the extinction cross-sections for the condensates in our models. In addition to our current application of the theory to exoplanetary atmospheric condensates, Mie theory has been widely used to study the observable effects of grain growth in the context of interstellar and circumstellar environments (Draine & Lee 1984; Stognienko, Henning & Ossenkopf 1995; Draine 2006). In particular, Mie theory and its variants have been recently employed to infer grain size distributions and compositions from spatially resolved submillimetre observations of protoplanetary discs (e.g. Tazzari et al. 2016).

2.2.1 Effective cross-section

An important feature of scattered irradiation is a strong angular asymmetry characterized by the phase function of scattered radiation. Except for very small particles of $\sim 10^{-2}$ μm , scattering (i.e. the phase function) of forward-propagating photons is favourably peaked in the forward direction. Indeed, larger particles produce sharper forward peaks. This angular asymmetry is largely due to the fact that radiations from the minute antennas in the forward direction are all in phase (Bohren & Huffman 1983).

Because the measured extinction at an observer is the theoretical extinction reduced by the scattered light collected by the detector,

the theoretical extinction cross-section is damped by the corresponding asymmetry parameter g characterizing the mean cosine of the scattering angle. The effective cross-section can thus be written as (Graaff et al. 1992; Van de Hulst 2003)

$$\sigma' \approx \sigma_{\text{ext}} - \sigma_{\text{scat}} g. \quad (11)$$

The limiting case of $g = 1$ (complete forward scattering towards the observer) recovers a cross-section due to thermalization of the grain alone, $\sigma' = \sigma_{\text{abs}}$. An asymmetry factor of nought is consistent with isotropy, with equal scattering both towards and away from the observer and thus $\sigma' = \sigma_{\text{abs}} + \sigma_{\text{scat}}$; scattered light with $g = -1$ is completely obscure to an observer and the total effective cross-section is an enhanced theoretical cross-section, $\sigma' = \sigma_{\text{ext}} + \sigma_{\text{scat}}$.

We show in Fig. 1 the effective extinction cross-section σ' of condensate species for modal particle sizes of $a_0 = 10^{-2}$, 10^{-1} and 1 μm calculated using our Mie theory code. The mean values of σ_{ext} , σ_{scat} and g are computed through equations (13) and (15), respectively. Groups of species have common features in the IR due to similar chemical bonds and thus similar energy-level excitations. The works of Lecavelier Des Etangs et al. (2008) and Wakeford & Sing (2015) use the total theoretical extinction cross-section σ_{ext} as the effective cross-section σ' and thereby overestimate the effective altitude $z_{\text{eff}}(\lambda)$ in transmission spectra, especially for large particle sizes, because the scattered spectrum for large particles is finely distributed around a scattering angle of 0 ($g = 1$). Moreover, the slope of the effective altitude is altered because σ_{scat} and g are both λ -dependent. Accounting for non-isotropic scattering is crucial, and the prescription we use here is a simple correction to include the effect of the angle-integrated scattering field.

2.3 Grain abundance

The abundance of the grains or aggregates containing the condensed species is ξ_{grain} . We assume grains to be composed purely of one condensate species. This assumes that homogeneous nucleation is more dominant than heterogeneous nucleation in the formation of condensates, but this may not be true across all atmospheres (cf. Marley et al. 2013). The grain abundance in equation (4) is

$$\xi_{\text{grain}} = \frac{3\xi_{\text{main}}\mu_{\text{cond}}}{2\rho_{\text{grain}}\pi a^3}. \quad (12)$$

A derivation of this equation can be found in Appendix C. Here, μ_{cond} is the mean molecular mass of the condensate species; ξ_{main} is the solar abundance of the dominant atomic species in the condensate, for which values are acquired from Burrows & Sharp (1999); and ρ_{grain} is the grain density of the species.² These chemical characteristics together with the approximate cloud condensation temperatures at ~ 1 mbar are shown in Table 1 for the set of 12 condensate species.

2.4 Particulate size distribution

The discussion has heretofore assumed a single particle size. However, atmospheres are not composed of one standardized particle size but generally contain condensate grains of many dimensions collectively referred to as polydispersions. We here discuss how we incorporate size distributions into our numerical model for transmission spectra.

¹ We make our Mie theory condensate data publicly available at www.github.com/exo-worlds/Mie_data.

² The grain densities are extracted from http://webmineral.com/Alphabetical_Listing.shtml#.V5nTr451o9g.

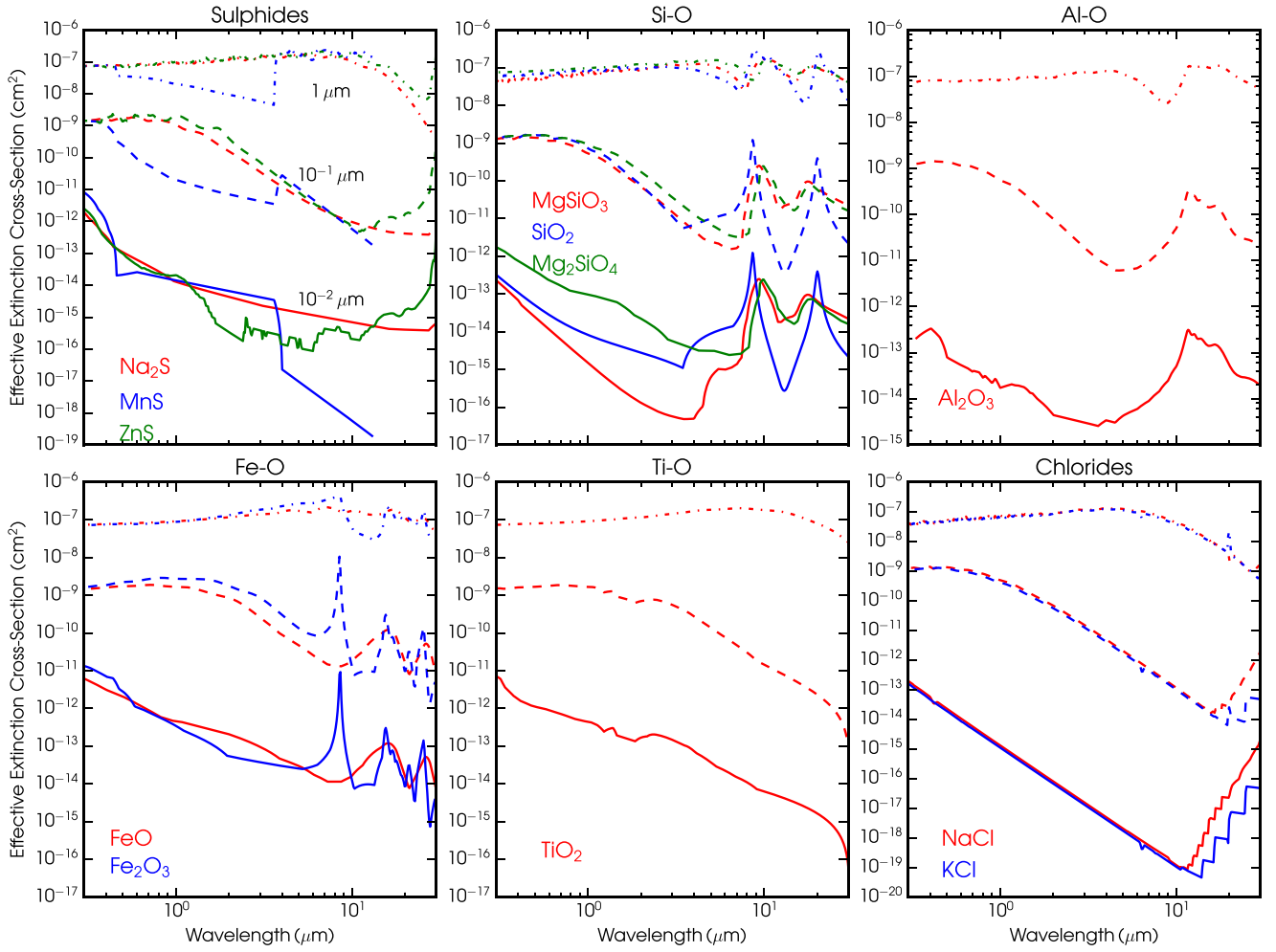


Figure 1. Effective cross-sections σ' of condensates considered in this work calculated using our Mie theory code. Shown are the cross-sections for modal particle sizes of 10^{-2} μm (solid), 10^{-1} μm (dashed) and 1 μm (dot-dashed). We consider 12 condensate species with refractive index data from ~ 0.3 μm redwards, grouped into chemical types.

Table 1. Properties of the 12 condensate species considered in this work. The prominent elemental abundances are adopted from Burrows & Sharp (1999) whilst the condensation temperatures are obtained from Wakeford & Sing (2015) for a pressure of 10^{-3} bar.

Condensate species	Condensation temperature (K)	ξ_{main}	Mean molar mass (g mol^{-1})	Density (g cm^{-3})
Na_2S	1176	1.68×10^{-5}	78.04	1.43
MnS	1139	1.68×10^{-5}	87	4
ZnS	700	1.68×10^{-5}	97.45	4.05
MgSiO_3	1316	3.9×10^{-5}	100.33	3.2
SiO_2	1725	3.26×10^{-5}	60.08	2.62
Al_2O_3	1677	2.77×10^{-6}	101.96	4.05
FeO	1650	2.94×10^{-5}	71.79	5.7
Fe_2O_3	1566	2.94×10^{-5}	159.68	5.3
TiO_2	1125	7.83×10^{-8}	79.86	4.25
NaCl	825	1.87×10^{-6}	58.44	2.17
KCl	740	1.23×10^{-7}	74.55	2.17
Mg_2SiO_4 (Fe-rich)	1354	3.9×10^{-5}	140.63	3.27

2.4.1 Mean parameter values for size distribution

In order to consider particle size distributions, we compute mean values of the condensate properties. To do so, we weight the scattering and extinction cross-sections, the grain mixing ratio and the

asymmetry parameter by the normalized particle size distribution as follows,

$$\bar{\sigma}_{\{\text{ext}, \text{scat}\}} = \frac{\int_{a_1}^{a_2} \sigma_{\{\text{ext}, \text{scat}\}}(a; \lambda) n(a) da}{\int_{a_1}^{a_2} n(a) da} \quad (13)$$

and

$$\bar{\xi}_{\text{grain}} = \frac{\int_{a_1}^{a_2} \xi_{\text{grain}}(a)n(a)da}{\int_{a_1}^{a_2} n(a)da}, \quad (14)$$

and

$$\bar{g}(\lambda) = \frac{\int_{a_1}^{a_2} g(a; \lambda)n(a)da}{\int_{a_1}^{a_2} n(a)da}, \quad (15)$$

where $n(a)$ is the number of particles in unit volume with radii between a and $a + da$ and $g(a; \lambda)$ is the asymmetry parameter for one particle size. Implicit in the above equations is the assumption that the scattering process at one particle is not influenced by other particles. To compute $g(a; \lambda)$, there are two elements of the scattering matrix that are important to calculate the intensity of light in any scattered direction. S_1 and S_2 describe the angular distribution of scattered light assuming unpolarized incident radiation expected from exoplanet host stars. These elements are calculated according to Deirmendjian (1969),

$$S_1 = \sum_{n=1}^{\infty} \frac{2n+1}{n(n+1)} \{a_n \tau_n(\cos \theta) + b_n \tau_n(\cos \theta)\}, \quad (16)$$

$$S_2 = \sum_{n=1}^{\infty} \frac{2n+1}{n(n+1)} \{a_n \tau_n(\cos \theta) - b_n \tau_n(\cos \theta)\}, \quad (17)$$

where $\pi_n(\cos \theta) = P_n(\cos \theta)/\sin(\theta)$ and $\tau_n(\cos \theta) = \frac{d}{d\theta} P_n(\cos \theta)$ are functions of Legendre polynomials P_n . These Mie scattering coefficients can also be generated via their own recursion relations without explicit reference to the underlying Legendre polynomials so as to be more useful for our numerical computations. The recursion relations for these angular functions are (Bohren & Huffman 1983)³

$$\pi_n(\theta) = \cos \theta \frac{2n-1}{n-1} \pi_{n-1}(\theta) - \frac{n}{n-1} \pi_{n-2}(\theta) \quad (18)$$

$$\tau_n(\theta) = n \cos(\theta) \pi_n(\theta) - (n+1) \pi_{n-1}(\theta) \quad (19)$$

with zeroth, first and second values as

$$\pi_{-1}(\theta) = 0$$

$$\pi_0(\theta) = 1$$

$$\pi_1(\theta) = 3 \cos(\theta) \quad \text{and} \quad \tau_{-1}(\theta) = 0$$

$$\tau_0(\theta) = \cos(\theta)$$

$$\tau_1(\theta) = 3 \cos(2\theta). \quad (20)$$

The scattered intensity in an angular direction θ characterizing the deflection from the original photon direction can be quantified in terms of a probability density function $p(\theta, a)$ called the phase function as (Box 1983)

$$p(\theta, a) = 2\pi\lambda^2 \frac{(|S_1|^2 + |S_2|^2)}{\sigma_{\text{scat}}}. \quad (21)$$

The phase function is normalized such that the integral of this probability density function over all solid angles $d\omega = \sin \theta d\theta d\phi$

³ The expression for π_n differs from Deirmendjian (1969)'s by a multiplicative factor of n in the numerator of the third term. In addition, Deirmendjian (1969)'s expression for $\tau_n(\theta)$ is shown to be in error and has been corrected here.

is 4π . The asymmetry parameter $g(a; \lambda)$ is then incorporated into equation (15) as

$$g(a; \lambda) = \frac{\int_0^\pi \int_0^{2\pi} p(\theta; a) \cos(\theta) d\omega}{\int_0^\pi \int_0^{2\pi} p(\theta; a) d\omega}. \quad (22)$$

2.4.2 Functional form of particle size distribution

Spectra of planetary atmospheres have been fitted by various particle size distributions, such as lognormal distributions, gamma distributions and power laws. The particle distribution we use is the modified gamma distribution (Deirmendjian 1964) whose general form is

$$n(a) = \omega a^\beta e^{-ba^\alpha} \quad (23)$$

and derives its name from the fact that the canonical gamma distribution is recovered for $\alpha \equiv 1$. Here ω , β , b and α are positive real numbers with the addition that α is an integer. Particular solutions of this general form are infinite and therefore the choice of which to use must involve justification. We use a particular form of the generalized form (Budaj et al. 2015),

$$n(a) = \left\{ \frac{a}{a_0} \right\}^6 e^{-6a/a_0}, \quad (24)$$

where a_0 is the modal particle size of the distribution. Deirmendjian (1964) justifies the use of the generalized and specific forms in stating that a survey of the many proposed functional forms shows that this particular form of the general modified distribution fits well with measurements of Earth's water clouds and aerosols for $a_0 \approx 4 \mu\text{m}$, and has the advantage that its parameters have more physical connotations than other distributions. Given the impossibility of *in situ* measurements of cloud particle sizes in exoplanetary atmospheres, the assumed distribution appears a reasonable assumption at present. Given the great variety of nature, however, it is expected that the exact cloud particle size distributions in exoplanetary atmospheres will naturally deviate from that assumed.

2.5 Free parameters

Our transmission spectrum model contains five free parameters as follows.

(a) Cloud scaleheight, H_c : Most planets in the Solar system including Earth have cloud scaleheights $H_c \lesssim H/3$ (Carlson, Lacis & Rossow 1994; Brooke et al. 1998; Ackerman & Marley 2001; Sánchez-Lavega, Pérez-Hoyos & Hueso 2004; Fortney 2005). Yet dynamical mixing processes in hot Jupiter atmospheres allow considerable deviations from these local findings (Parmentier, Showman & Lian 2013), especially for small grains that do not settle readily. Varying H_c has important ramifications on the transit depth or effective altitude. Decreasing the value of H_c effectively decreases the condensate opacity and hence tends the slope towards the gaseous Rayleigh limit and also lowers the continuum level of the transmission spectrum.

(b) Modal particle size, a_0 : Particle sizes in planetary atmospheres are expected to be distributed over a continuum of sizes. We assume that cloud particles follow a certain distribution with a modal size. Increasing the modal size decreases the slope of the transit spectrum, with a tendency towards flat spectra for the very largest of particle sizes.

(c) Reference pressure, p_0 : The pressure associated with the inferred radius R_{p_0} can range from ~ 1 to $\sim 10^{-3}$ bar. Increasing

(decreasing) p_0 shifts R_{p_0} lower (higher) in the planet, increasing (decreasing) the transit depth level.

(d) Grain abundance, ξ_{grain} : The non-equilibrium nature of cloud condensation makes determining the grain abundance $n_{c,i}/n_{\text{tot},i}$ difficult and uncertain. We have assumed that the homogeneous grains are limited by the dominant element of the condensate species (cf. Lecavelier Des Etangs et al. 2008; Wakeford & Sing 2015).

(e) Molecular abundance, ξ_j : The molecular abundances of different volatile species have been suggested to range from sub-solar to supersolar (Fortney et al. 2013; Kreidberg et al. 2014b; Madhusudhan et al. 2014, 2016; Mordasini et al. 2016; MacDonald & Madhusudhan 2017). We investigate different molecular abundances with cloud types in Section 3.3 to determine significant IR features observable with future *JWST* spectra.

3 RESULTS

We have developed a model for transmission spectra of cloudy atmospheres. We show a number of its applications to observations following three key observables. We first construct a metric characterizing the slope of the transmission spectrum in the 0.3–0.56 μm spectral range. This metric can be useful for constraining cloud compositions, scaleheights and modal particle sizes using high-precision observations. Moreover, we discuss the use of temperature information as a way to reduce degeneracies amongst the different cloud properties. We then continue with a discussion on the uniformity of slopes in the optical as an additional way to break degeneracies using high-precision observations. Finally, we show which condensate features are pronounced in the IR as a means to identifying dominant cloud signatures with future *JWST* spectra.

3.1 A metric to evaluate optical slopes

Transmission spectra of exoplanets in the visible show various slopes that hint towards the existence of different cloud species. We here construct a metric to extract cloud information from the observed spectrum in the optical window of 0.3–0.56 μm . We find this window to be the best metric for the optical slope since it avoids potential contributions from the gaseous sodium and potassium absorption features at approximately 0.59 and 0.77 μm . It is possible that other species could have spectral features in this range, e.g. TiO and VO (Hubeny, Burrows & Sudarsky 2003). However, detections of such species are still tentative (see e.g. Evans et al. 2016), and planets with T_{eq} below 2000 K are less likely to host high-temperature gases such as TiO and VO (Hubeny et al. 2003). We have considered using the slopes between 0.6 and 0.8 μm as a second metric window, neglecting the Na and K features. Using this latter window, however, is not a good predictor of the properties for single species unless the slope in the entire optical is nearly constant.

Observations of hot Jupiter atmospheres obtain the transit depth Δ from which the total radius of the planet R_{p_λ} as a function of wavelength is extracted. The slope of this observed radius is then

$$m_{\text{obs}} = \frac{dR_{p_\lambda}}{d\ln\lambda} = \gamma H_c. \quad (25)$$

Here there is a degeneracy in the slope for values of γ and H_c . Because the cloud scaleheight H_c is generally difficult to determine a priori, the slope should be formulated in terms of the more certain bulk atmospheric scaleheight H . The slope of $R_{p_\lambda} = (R_{p_0} + z_{\text{eff}})$

expressed in a more convenient dimensionless form is

$$\begin{aligned} \mathcal{S} &\equiv \frac{m_{\text{obs}}}{H} = \frac{d(R_{p_\lambda}/H)}{d\ln\lambda} \\ &= \frac{d(z_{\text{eff}}/H)}{d\ln\lambda} = \gamma \frac{H_c}{H}, \quad \text{for } 2H/5 \lesssim H_c \leq H. \end{aligned} \quad (26)$$

In the limit of small H_c ($H_c \lesssim 2H/5$), \mathcal{S} tends to -4.2 due to Rayleigh scattering from ambient H_2 . The dimensionless slope \mathcal{S} is determined through dividing the directly observable quantity m_{obs} by the atmospheric scaleheight H . The scaleheight H is typically taken to be the equilibrium scaleheight, such that $H = H_{\text{eq}} = k_B T_{\text{eq}} / (\mu g)$ where the equilibrium temperature obtained from radiative balance is (Seager 2010)

$$T_{\text{eq}} = T_* \left(\frac{R_*^2}{2a_{\text{major}}^2} \right)^{1/4} (f(1-A))^{1/4}, \quad (27)$$

in which a_{major} is the semi-major axis of the planet, A is the Bond albedo and f is the heat redistribution fraction. The equilibrium temperature defines an upper bound for the assumed scaleheight H since the temperature in the terminator region of the atmosphere as observed in transmission spectra may be safely assumed to be smaller than T_{eq} .

The observer measures a slope m_{obs} and divides by an estimate for H to get the slope in the dimensionless form as in equation (26). The new slope \mathcal{S} therefore involves a directly observable quantity and an estimated quantity and is thereby sensitive to changes or uncertainty in H . The deviation in \mathcal{S} due to an uncertainty in the value H from the actual value is written as

$$\frac{\delta\mathcal{S}}{\mathcal{S}} = -\frac{\delta H}{H}. \quad (28)$$

The uncertainty in bulk atmospheric scaleheight H enters through uncertainty in the temperature T and the mean molecular weight μ . Assuming knowledge of μ , the primary source of uncertainty is in T such that $-\frac{\delta H}{H} = -\frac{\delta T}{T} = -\frac{T_{\text{act}} - T_{\text{es}}}{T_{\text{es}}}$. The actual temperature in the observable atmosphere at the terminator T_{act} is always likely to be less than the estimated temperature $T_{\text{es}} (=T_{\text{eq}})$, such that δT is negative giving a negative $\delta\mathcal{S}$ for a negative \mathcal{S} . For example, if the actual temperature is lower than $T_{\text{es}} = T_{\text{eq}}$ by 25 per cent ($\delta T/T_{\text{eq}} = -0.25$) and $\mathcal{S} = -4$, then the slope can only change by -1 , i.e. $\delta\mathcal{S} = -1$. Therefore, the dimensionless slope \mathcal{S} does not significantly change even for reasonably large δT . On the other hand, knowledge of T subsumes ignorance into μ , giving instead $-\frac{\delta H}{H} = -\frac{\delta\mu}{\mu}$. Assuming that H_2O constitutes the only metallic component, the uncertainty in \mathcal{S} for an atmosphere of $50 \times$ solar metallicity for which H is estimated with a solar-metallicity assumption translates to $\delta\mathcal{S} = +0.8$.

In the present work, we focus on H_2 -rich atmospheres that have the most observations. In particular, we focus on transiting hot Jupiters and therefore the mean molar mass of the atmosphere and gravity are taken as fiducial with $\mu = 2.3 \text{ g mol}^{-1}$ and $g = 24.79 \text{ m s}^{-2}$. Throughout our work, we take the background temperature profile to be an isotherm set to the equilibrium temperature of the planet. We also take the cloud base to be coincident with the bottom of the atmosphere at 10 bar, similar to assumptions from previous studies (cf. Lecavelier Des Etangs et al. 2008). The computed best-fitting slopes \mathcal{S} of the transmission spectra in the 0.3–0.56 μm range for the different condensates are shown in Fig. 2. The slopes are computed for atmospheres of single cloud species together with H_2 Rayleigh scattering and for a range of scaleheights and modal particle sizes in the modified gamma distribution. Neither variations in g , p_0 nor R_{p_0} make any difference

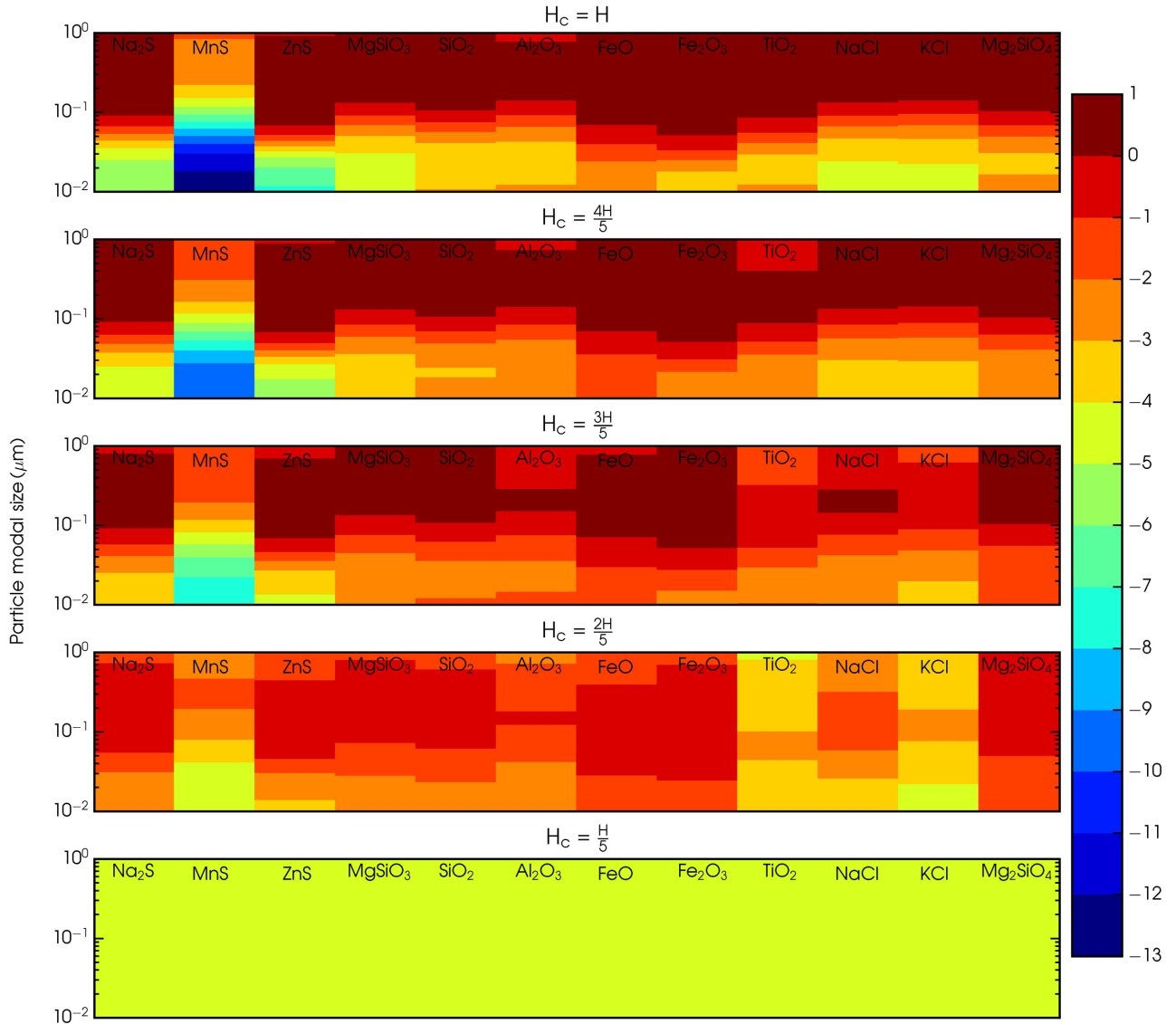


Figure 2. Best-fitting slopes \mathcal{S} of the transmission spectrum z_{eff}/H (see Fig. 3) in the window $0.3\text{--}0.56\ \mu\text{m}$ for the 12 condensate species of various modal sizes and H_2 Rayleigh scattering. The transmission spectrum z_{eff}/H is calculated using equations (4)–(6). The panels show atmospheres with cloud scaleheights of $H_c = H, 4H/5, 3H/5, 2H/5$ and $H/5$.

on the computed slope values. Once $H_c \lesssim 2H/5$ is reached in Fig. 2, the rapid fall of the cloud number density with height means that the H_2 Rayleigh scattering slope begins to dominate in the optical. The condensate contribution continues to diminish in progression towards lower H_c and the slope meets a value of -4.2 typical of equation (5) at $H_c \approx 0.2H$. The cloudy models in Fig. 3 show transmission spectra for $a_0 = 10^{-2}\ \mu\text{m}$. The progression $H_c = H \rightarrow H/5$ is made clear, where clouds dominate for large scaleheights while H_2 Rayleigh scattering dominates for low H_c irrespective of cloud composition. Fig. 2 is useful in showing the degeneracy of cloud properties (e.g. composition, modal particle size and scaleheight) commensurate with an observed slope.

There are several important points to be extracted from Fig. 2 as follows.

(a) Sulphides are the only species considered over all modal particle sizes and scaleheights for which $|\mathcal{S}| > 5$. Observations showing

steep slopes of $|\mathcal{S}| > 5$ suggest sulphide clouds Na_2S , MnS and ZnS .

(b) Effects of homogeneous clouds in transmission are observable in the optical for $H_c \gtrsim 0.4H$. Values of H_c less than $0.4H$ suggest two possibilities. $H_c/H \lesssim 0.4$ may suggest the presence of inhomogeneous or patchy clouds (see Section 4 for an application of this idea to the optical spectrum of HD 209458b) or H_2 Rayleigh scattering as the dominant culprit.

(c) It is possible to obtain properties of condensate species commensurate with an observed slope when $0.4H \lesssim H_c \leq H$ if we have good knowledge of the p – T profile in the atmosphere. The current state of observations allows for slope degeneracies over cloud composition, scaleheight and modal particle size. Large particles (having low γ , due to a grey σ' approached in the geometric limit of Mie theory) with large scaleheights are degenerate in slopes with small particles (high γ , Rayleigh limit) with small scaleheights. Unless a more definite calculation for H_c is achieved, this latter degeneracy remains present.

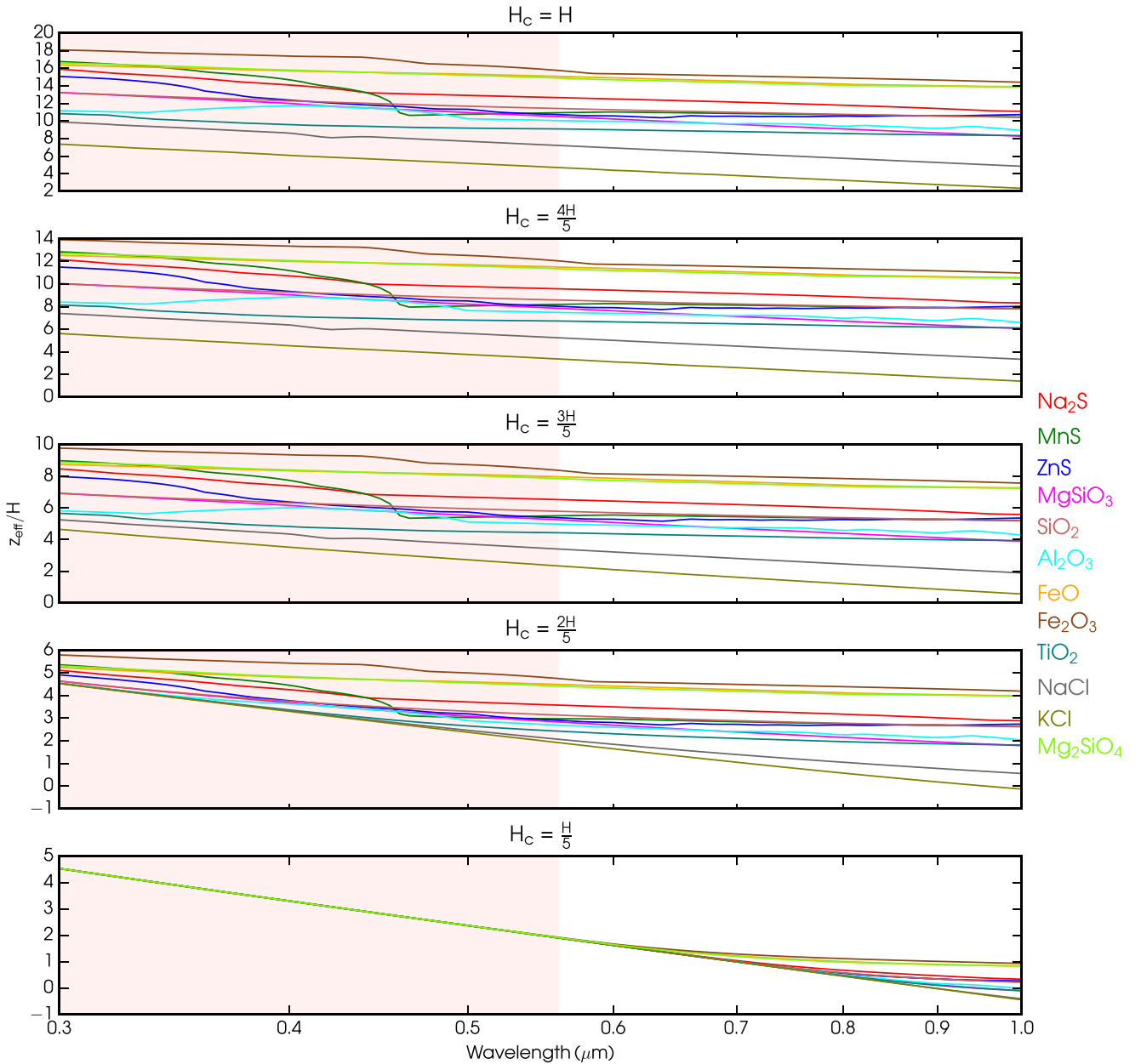


Figure 3. The transmission spectrum z_{eff}/H for the 12 condensate species with $a_0 = 10^{-2} \mu\text{m}$ and H_2 Rayleigh scattering calculated through equation (4)–(6). The panels show atmospheres with respective cloud scaleheights of $H_c = H, 4H/5, 3H/5, 2H/5$ and $H/5$ that associate with the panels of Fig. 2. The light red area shows the region $0.3\text{--}0.56 \mu\text{m}$ from which the slopes in Fig. 2 are calculated.

(d) A slope of -4 does not of itself imply H_2 Rayleigh scattering, as such a slope is reproduced by some clouds (e.g. sulphides and chlorides, see Fig. 2) with large scaleheights especially in the Rayleigh regime for $a_0 \approx 10^{-2} \mu\text{m}$ (see discussion in Section 3.2).

3.1.1 Using temperature to break degeneracy

The temperature structure of the atmosphere can be used as a guide to predict which cloud species are able to condense and thereby reduce degeneracies amongst cloud properties. To first order, clouds are formed when the temperature of the atmosphere becomes colder than the saturation vapour temperature of a species at a given pressure. The temperature structure can be obtained in the first place

by retrieval on observations in primary transit or secondary eclipse (Madhusudhan & Seager 2009; Madhusudhan et al. 2011; MacDonald & Madhusudhan 2017). Here we use Fig. 2 to illuminate a few important features for the interpretation of transmission spectra assuming knowledge of the atmospheric temperature at ~ 1 mbar. We note that using the temperature structure alone neglects other processes that may be active in the atmosphere such as spatial mixing of condensates that can loft deep-forming clouds into the observable atmosphere, complicating a distinct interpretation (Parmentier et al. 2013). Nevertheless, below we use the cloud condensation temperatures in the observable atmosphere as shown in Table 1 to make predictions about possible cloud properties.

$T \approx 700$ K: If the temperature at ~ 1 mbar is determined to be less than 700 K from the p - T profile, ZnS (zinc sulphide) and KCl (potassium chloride) may dominate as condensates in the accessible atmosphere. If observations show a slope of $\mathcal{S} < -4$, ZnS clouds may exist in the atmosphere described by modal sizes of $a_0 \approx 10^{-2}$ – 3×10^{-2} μm and $H_c \approx H$ or KCl clouds with sizes 10^{-2} – 2×10^{-2} μm . As the cloud scaleheight is decreased to $H_c = 4H/5$, slopes decrease correspondingly by $4/5$. An important trend that is present for all condensate species is that slopes for large cloud scaleheights with large modal particle sizes are mimicked by lower cloud scaleheights from smaller modal particle sizes. For example, KCl particles with a modal size of ~ 0.08 μm assuming $H_c = H$ produce the same slope interval of -1 to -2 as KCl clouds with $H_c = 3H/5$ with modal sizes of 0.05 μm . This trend follows from a ready understanding of equation (26): a large modal size (a low γ) coupled with a large H_c/H gives the same slope as a small modal size (a high γ) coupled with a small H_c/H . This degeneracy is always present unless there exists a direct method to predict H_c/H . A first-order approximation to H_c/H derived from first principles is Sánchez-Lavega et al. (2004)'s equation 22. This equation might be utilized to further constrain the cloud species and modal size responsible for the observed optical slope.

$T \approx 800$ K: If observations show a slope of $-5 < \mathcal{S} < -3$, NaCl should be well mixed in the planetary atmosphere and contain grain modal sizes of between 10^{-2} and 5×10^{-2} μm . The slopes decrease with gradually decreasing H_c by the appropriate fractions. Scattering by molecular hydrogen begins to occur at $H_c \approx 2H/5$ and a pure Rayleigh slope is achieved at $H_c \approx H/5$.

$T \approx 1100$ K: If $\mathcal{S} \lesssim -8$, MnS (manganese (II) sulphide) may exist in the atmosphere for which a direct constraint on the modal size can be determined with the addition that $H_c = H$. On the other hand, there are alternative possibilities if the atmospheric temperatures at ~ 1 mbar are thought to be conducive for MnS clouds but observations show slopes of $-8 \lesssim \mathcal{S} \lesssim -3$. Na₂S (sodium sulphide), MnS and/or TiO₂ (titanium dioxide) may exist in the atmosphere. Observations well fitted with a straight line leave Na₂S as the responsible condensate against MnS and TiO₂ (see discussion in Section 3.2). If $\mathcal{S} \gtrsim -3$, there is a degeneracy that arises in that the slopes could be produced either by large particles with $H_c \approx H$ or by small particles with scaleheights of $H_c \approx 3H/5$. There is a general pattern in that per given slope, the modal size producing this slope increases sequentially for TiO₂, Na₂S and MnS, respectively. Once the scaleheight becomes lower than $H_c \approx 2H/5$, the magnitude of H₂ scattering dominates and the spectrum resembles that of a pure H₂ atmosphere by $H_c = H/5$.

$T \approx 1300$ K: Observed slopes of $\mathcal{S} \lesssim -4$ suggest the existence of MgSiO₃ clouds with modal sizes between 10^{-2} and 3×10^{-2} μm mixed well with the gas. Mg₂SiO₄ (forsterite) always has a shallower slope than enstatite for given H_c and a_0 .

$T \approx 1500$ K: Slopes of $-4 \lesssim \mathcal{S} \lesssim -2$ implicate Fe₂O₃ (iron (III) oxide) with modal sizes 10^{-2} – 3×10^{-2} μm with $H_c \approx H$. Slopes larger than -2 show a degeneracy for different H_c - a_0 combinations until $H_c = 2H/5$, at which point the slopes begin to approach a molecular H₂ value of -4 .

$T \approx 1600$ K: Gradients \mathcal{S} between -3 and -4 suggest Al₂O₃ (alumina) rather than FeO (iron oxide) as the condensate species; moreover, these alumina particulates have sizes of about 2×10^{-2} μm with a scaleheight of H . Slopes lying between -2 and -3 may be due to either cloud type with modal sizes of 10^{-2} – 2×10^{-2} μm for FeO or 5×10^{-2} μm for alumina, with either option having a scaleheight of nearly H .

$T \approx 1700$ K: If $-4 \leq \mathcal{S} \leq -3$, SiO₂ (silicon dioxide) may be well mixed in the atmosphere with modal sizes between 10^{-2} and 4×10^{-2} μm , whilst an \mathcal{S} between -2 and -3 constrains the modal size to 5×10^{-2} μm . The slopes and modal sizes for $H_c = 4H/5$ and $3H/5$ are almost indistinguishable and remain degenerate unless a physically independent computation of H_c is achieved.

3.2 The uniformity of cloud optical slopes

Most current models of transit spectra use parametric prescriptions for clouds in the optical in both forward models and retrievals resulting in constant slope values (e.g. Sing et al. 2016). Observations of current precisions can generally be fitted by cloud types with uniform-slope parametric prescriptions. In this section, we explore the uniformity of slopes in the optical for different cloud species. The uniformity of the scattering slopes in the visible provides an additional broad constraint on the condensate composition of special importance for high-precision observations.

We show the transmission spectra of all 12 condensates with $H_c = H$ for three modal particle sizes (0.01, 0.1 and 1 μm) in Fig. 4. The value $H_c = H$ best highlights the differences between species with non-linear and uniform linear spectra. The condensates fall into two groups according to whether a uniform slope is displayed in the optical range of 0.3–0.8 μm . Our definition of ‘uniform’ is informed by observations. We start at the lowest wavelength and construct a 1σ envelope with the same slope as that at the lowest wavelength. A model curve that is able to fit completely within this 1σ envelope is considered to have a uniform slope. The average 1σ uncertainty in z_{eff}/H for the 10 hot Jupiters in Sing et al. (2016) is ~ 1.25 , which we use here.

A small number of condensates of modal sizes $\sim 10^{-2}$ μm have non-uniform slopes in the optical. As shown in Fig. 4, MnS, ZnS, Fe₂O₃ and TiO₂ have the most significant changes in the scattering and absorption properties in the optical leading to large variations in transit spectrum slopes. MnS deviates from uniformity most significantly with a broad valley at 0.5 μm . Fe₂O₃ shows three distinct regions composing different slopes, and TiO₂ has a smoother dip than MnS that extends over the whole visible range. On the other hand, high-precision observations showing no significant non-linearity in the visible can reduce species degeneracy to one or more species in the bottom group in Fig. 4. Increasing the grain modal particle size to 0.1 μm leads to an essentially grey opacity for all species in the optical except for MnS. For even larger modal particle sizes of ~ 1 μm , flat spectra result for all cloud species.

In summary, small modal particle sizes of ~ 0.01 μm produce non-flat spectra. Non-uniform and non-flat spectra are caused by a select few species of MnS, ZnS, Fe₂O₃ and TiO₂. Particle distributions with greater modal sizes of $\gtrsim 0.1$ μm produce flat, uniform spectra essentially for all cloud types.

3.3 Cloud features in the IR

The transit spectrum in the IR has great potential to reduce degeneracies through identification of condensate signatures. On the other hand, IR spectra could be dominated by absorption features due to volatile species, e.g. water vapour. We study cloud signatures for different combinations of H₂O abundances and modal particle sizes to identify condensate features that are observable in IR spectra, e.g. with *JWST*. We generate model transit spectra of cloudy hot Jupiter atmospheres with a representative isothermal temperature of 1450 K.

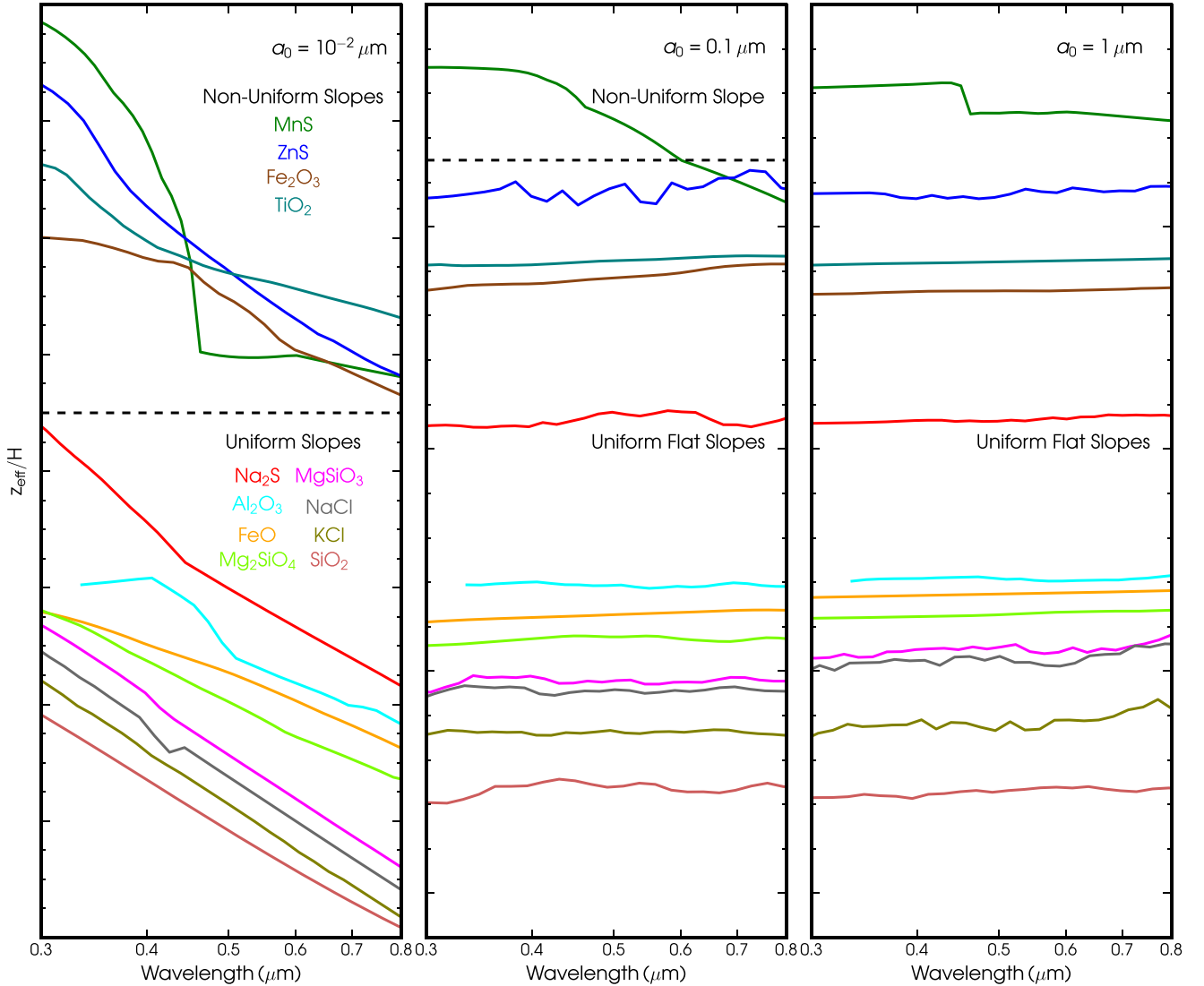


Figure 4. Model transmission spectra of condensate species showing linear and non-linear trends for three modal particle sizes assuming $H_c = H$. All condensates but MnS, ZnS, Fe_2O_3 and TiO_2 display observationally limited linear slopes. The dashed black horizontal line delineates between cloud types showing non-uniform and uniform slopes. Vertical offsets have been applied to make these delineations clear.

The abundance of H_2O and the modal sizes of cloud particles determine the amplitudes and appearances of condensate features in the IR. Fig. 5 shows transmission spectra for six sets of conditions spanning H_2O abundances of $10^{-2} \times$ solar, solar and $100 \times$ solar and a_0 of 10^{-2} and $1 \mu\text{m}$. These spectra were calculated with additional opacities of CIA $\text{H}_2\text{--H}_2$ and CIA $\text{H}_2\text{--He}$ in equation (4) assuming $H_c = H$. The six combinations illuminate significant condensate signatures that are observable with high-precision and high-resolution spectra in the IR.

(a) Solar H_2O , small a_0 : Fig. 5 shows four cloud species dominate the spectrum for small particulates contained in high H_2O abundances at solar value. These species are SiO_2 , Fe_2O_3 , MgSiO_3 and Mg_2SiO_4 . SiO_2 and Fe_2O_3 have strong spectral features at $8\text{--}9 \mu\text{m}$, and MgSiO_3 and Mg_2SiO_4 have overlapping absorption signatures at $\sim 10 \mu\text{m}$. However, given the lower condensation temperature of Fe_2O_3 compared to SiO_2 , distinguishing between these two species may be possible. On the other hand, MgSiO_3 and

Mg_2SiO_4 have similar condensation temperatures. Distinguishability between these may come from the amplitude between optical and IR observations, with MgSiO_3 possessing a larger amplitude by a factor of ~ 4 . All four features are of special interest because they occur in a region around $\sim 10 \mu\text{m}$ where there is little contribution from H_2O absorption, i.e. the valley between the two H_2O peaks.

(b) Subsolar H_2O , small a_0 : Lower abundances of water vapour with efficiently scattering small particulates bring out more subtle features for the four condensates compared with state (a). SiO_2 , Fe_2O_3 , MgSiO_3 and Mg_2SiO_4 show multiple features, having additional signatures at wavelengths beyond $\sim 12 \mu\text{m}$. MgSiO_3 and Mg_2SiO_4 have overlain features at $\sim 18 \mu\text{m}$ that may again be distinguished by the difference in optical-IR amplitudes. An SiO_2 peak at $19 \mu\text{m}$ lies in the valley between two prominent Fe_2O_3 peaks at ~ 15 and $\sim 22 \mu\text{m}$, helping to safely distinguish between potential observations in the $\sim 8 \mu\text{m}$ region. The steep MnS feature at $\sim 4 \mu\text{m}$ is significant due to its enlargement of the optical-IR amplitude.

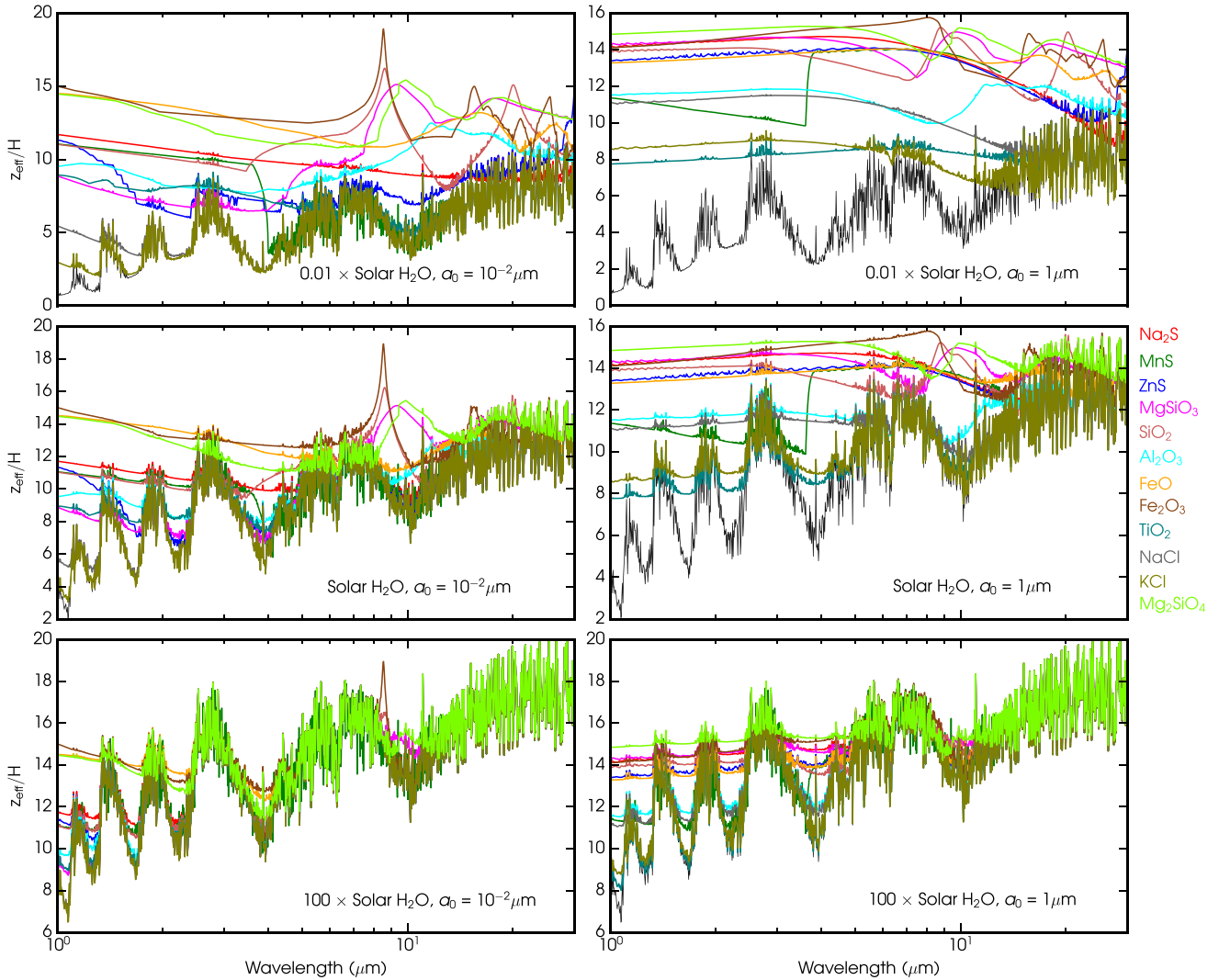


Figure 5. Model transmission spectra of cloudy hot Jupiter atmospheres with different condensate compositions. The models also contain opacity due to H_2O , $\text{H}_2\text{--H}_2$ CIA and $\text{H}_2\text{--He}$ CIA in the IR. Each panel represents a particular size distribution and atmospheric H_2O abundance and assumes $H_c = H$. The black curves show reference cloud-free models with appropriate H_2O abundances for each panel.

(c) Solar H_2O , high a_0 : Large modal particle sizes in solar abundance atmospheres produce a similar narrative to (a). The main effect of increasing particle dimensions is to transition Mie theory into the geometric limit. The extinction coefficient for large modal sizes approaches a constant value, as seen by the $1\ \mu\text{m}$ curves in Fig. 1. The effect is to broaden the narrow features characteristic of small modal sizes. Interestingly, the MnS feature at $\sim 4\ \mu\text{m}$ is inverted relative to case (b). This feature is remarkable because it is not due to absorption as is generally assumed of all condensate features in the IR (Wakeford & Sing 2015). The scattering and absorption refractive indices for MnS illustrate that this feature is due to strong scattering for particle sizes of $\gtrsim 0.1\ \mu\text{m}$ (see MnS panel in fig. 1 of Wakeford & Sing 2015). The case of MnS demonstrates the mistake of this typical assumption, suggesting that scattering may indeed dominate features in the IR for other cloud species not considered in this work.

(d) Subsolar H_2O , high a_0 : Transit spectra of atmospheres with depleted water abundances and large dominant cloud particles are relatively flat with low-amplitude features. As in (c), the amplitudes of condensate signatures are quenched with respect to smaller

particles but the multiple spectral features of different species in (b) are present. The Al_2O_3 attribute from $\sim 10\text{--}20\ \mu\text{m}$ exists only for subsolar water abundances and across all particle sizes. As observed by Wakeford & Sing (2015), sulphides and chlorides are seen to have no prominent features in the mid-IR at wavelengths beyond $\sim 4\ \mu\text{m}$.

(e) Supersolar H_2O : Highly supersolar ($100\times$) H_2O abundances generally supersede all cloud features in the IR. For small modal particle sizes, the vibrational absorption peak of Fe_2O_3 at $\sim 9\ \mu\text{m}$ is still distinguishable from the large-amplitude H_2O features. On the other hand, no cloud features are present for large modal sizes. Condensates for which the opacity is large compared to the H_2O opacity, e.g. due to large modal particle sizes, exhibit flat spectra in the NIR.

As realized by our Fig. 5 and in Wakeford & Sing (2015), sulphide and chloride spectral features are not present even in the most promising scenario of subsolar H_2O abundances. This allows for spectral interpretation and predictions for planets suggested to host atmospheres with Na_2S , KCl and ZnS condensates, such

as GJ 1214b (Kreidberg et al. 2014a) and HD 95678b (Knutson et al. 2014b). Current observations of GJ 1214b and HD 95678b in transit using *HST Wide Field Camera 3 (WFC3)* in the NIR show spectra consistent with being flat. Our work suggests that this can be due to KCl condensates of 1 μm modal particle sizes and with subsolar water abundance. Moreover, Na_2S and ZnS can produce flat spectra for 1 μm modal sizes with subsolar to solar water abundances. *JWST* will be capable of observing the atmospheres of these planets at longer wavelengths than 2 μm . Our Fig. 5 predicts that future observations of GJ 1214b and HD 95678 should have transit depths that decrease towards longer wavelengths at $\gtrsim 9 \mu\text{m}$ if Na_2S , KCl and ZnS clouds indeed dominate the atmospheric spectra.

Our analysis of condensate signatures in the IR demonstrates four species to be the most conducive for spectroscopic identification with *JWST*: SiO_2 , Fe_2O_3 , MgSiO_3 and Mg_2SiO_4 . MnS also has a distinct feature at 4 μm but shows no observable features at longer wavelengths. Three instruments aboard *JWST* will be important for transmission spectroscopy in the IR: the Near Infrared Imager and Slitless Spectrograph (NIRISS), the Near Infrared Spectrograph (NIRSpec) and the Mid Infrared Instrument (MIRI). NIRSpec can operate in the window 0.6–5 μm in either low- or high- R ($\lambda/\Delta\lambda$) modes, and will be supplemented with NIRISS from 1.0 to 2.5 μm with low resolving power. These are complemented with MIRI in the window 5–29 μm with various spectral resolutions R , spanning low to high (Greene et al. 2016).

4 APPLICATION TO CURRENT OBSERVATIONS

We apply the metric from Section 3.1 to current observations of eight hot Jupiters. In particular, we discuss two hot Jupiters with the most precise observations, HD 209458b and HD 189733b. For the six other planets, we find that current precisions on the spectra allow for a degenerate set of solutions. The latter communicates the importance of improved precisions through multiple-orbit *HST* observations. Our models of HD 209458b and HD 189733b illustrate the need for more sophisticated cloudy transit models to interpret current high-precision spectra, as well as the need for higher quality data from future facilities such as *JWST* and ELTs.

Fig. 6 shows forward models compared with observations of eight hot Jupiters: WASP-17b, WASP-39b, HD 209458b, HAT-P-1b, WASP-31b, HD 189733b, WASP-6b and HAT-P-12b. Each panel shows the comparison for one planet and contains the computed best-fitting slope and its associated error in the window 0.3–0.56 μm for the observations of Sing et al. (2016). Sing et al. (2016) consider 10 hot Jupiters in their study. We do not include WASP-12b and WASP-19b in our study because their atmospheric temperatures are generally hotter than the condensation temperatures for species in Table 1. The suite of models for each planet are calculated assuming $H_c = H$ and the appropriate a_0 for each species using Fig. 2 that reproduces the central slope values of the Sing et al. (2016) observations (listed in Table 2). We assume an isothermal temperature profile valued at the equilibrium temperature of each planet as in Table 2. We choose $H_c = H$ for our models because condensate species are shown to experience strong mixing in hot Jupiter atmospheres (Parmentier et al. 2013). We are able to fit the observed spectra for the majority of hot Jupiters as seen in Fig. 6. The observed optical spectra in Fig. 6 contain large uncertainties, allowing for degenerate fits to transit observations ranging over different a_0 and cloud compositions. In particular, we find multiple indistinguishable fits for WASP-17b, WASP-39b, HAT-P-1b, WASP-31b, WASP-6b and HAT-P-12b.

We here show the importance of analysing spectra over a broad spectral range from the visible to mid-IR. As an example, we consider the case of MnS clouds for the transmission spectrum of WASP-6b. Fig. 2 of Sing et al. (2016) shows the planetary-averaged p – T profiles for the eight hot Jupiters along with solar-composition saturation vapour pressure curves. MnS is the only species for which the partial pressure exceeds the saturation vapour pressure in the observable atmosphere of WASP-6b. We compute the minimum χ^2 statistic for MnS by binning the model to the same resolution as the data over the three-dimensional set $\{p_0, H_c, a_0\}$, determining the best parameter set to be $\{0.02 \text{ bar}, 0.56H, 0.042 \mu\text{m}\}$. The bottom-left panel of Fig. 6 shows this best-fitting model (thick green curve) with a slope of -4.56 in the 0.3–0.56 μm window, with the best-fitting slope of the WASP-6b observations -4.14 ± 1.36 (see Table 2). Extended into the IR, however, this minimal χ^2 model is a poor fit with *Spitzer Infrared Array Camera (IRAC)* observations at 3.6 and 4.5 μm . Future cloud models should therefore always account for the entire spectrum simultaneously, especially in retrieval methods. A meaningful cloud statistical fit in one spectral region does not imply fits in other regions.

We now focus on two exoplanets with the most precise observations, HD 209458b and HD 189733b. The transmission spectra for HD 189733b and HD 209458b are shown in Fig. 7.

The observed spectrum of HD 189733b is a challenge to understand since it cannot be reproduced by any single condensate species. Two sulphide species, MnS and ZnS, fit the optical spectrum below 0.6 μm but slope upwards at longer wavelengths and hence provide a poor fit to the full spectrum overall. A preliminary investigation using combinations of composite species also shows poor fits with the observations. The work of Lecavelier Des Etangs et al. (2008) suggests that *HST* observations of HD 189733b by Pont et al. (2008) from 0.55 to 1.05 μm can be due alone to sub-micron MgSiO_3 particulates. On the other hand, Vahidinia et al. (2014)’s study of HD 189733b illuminates the important effects of cloud-condensate bases on transmission spectra and suggests that the steepness of the spectrum below the observed change in slope at $\lambda \approx 0.6 \mu\text{m}$ weakens the role of MgSiO_3 . Our work finds a similar conclusion to that of Vahidinia et al. (2014). We find that consideration of the steepness of the slope at wavelengths below 0.55 μm disfavors MgSiO_3 if the spectrum is assumed to originate from one species alone (see Fig. 7).

This may be a hint to looking at the host star’s variability. HD 189733b’s host star is active with a significant variation in photometry. Starspots and plagues can induce variations in the z_{eff}/H optical transmission spectrum (McCullough et al. 2014; Oshagh et al. 2014). A combination of plague occultations together with a few cloud-condensate species may well fit the observations. Another possibility is the existence of condensate species that have not been considered thus far.

On the other hand, the spectrum of HD 209458b allows for similar fits in the optical for nearly all cloud species as shown in Fig. 7. We also include a cloud-free model (black curve) with a water abundance of $0.01 \times$ solar. The cloud-free water model fits the observations in Fig. 7 best, whilst the homogeneous condensate spectra are unable to provide robust fits in the IR even with substantially supersolar water abundances. The poor fit between homogeneous cloud models and observations lends weight to a patchy cloud scenario, and consideration of the IR region with future *JWST* observations has potential to disambiguate the existence of condensate species. We here use a specific idea from our work to substantiate the first suggestion of inhomogeneous clouds on HD 209458b by MacDonald & Madhusudhan (2017). MacDonald &

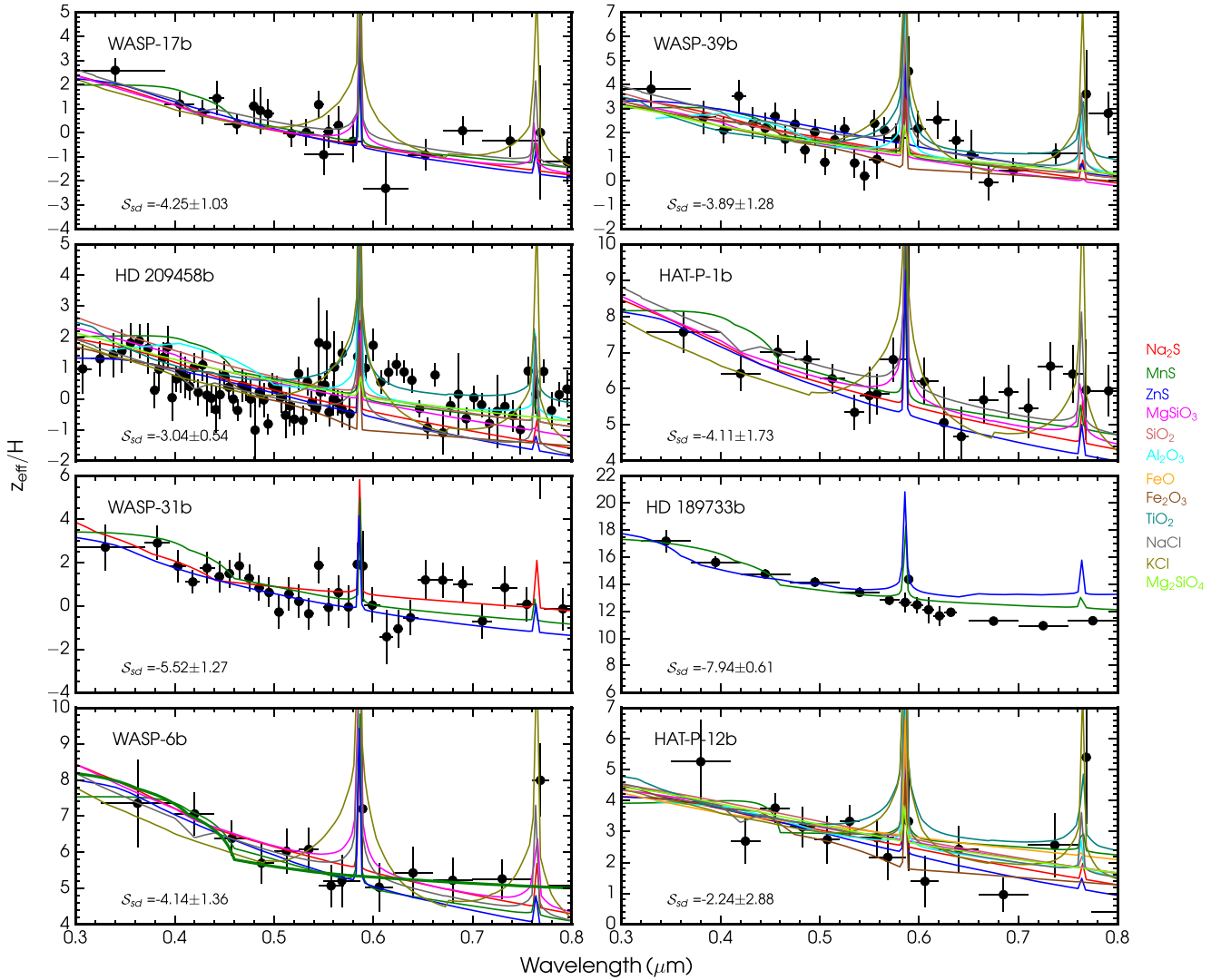


Figure 6. Forward models of condensate species compared with Sing et al. (2016) observations for a select eight hot Jupiters. From left to right, top to bottom: WASP-17b, WASP-39b, HD 209458b, HAT-P-1b, WASP-31b, HD 189733b, WASP-6b and HAT-P-12b. S_{scd} shows the slope of Sing et al. (2016) data with its associated uncertainty in the window 0.3–0.56 μm . The thick green curve in the bottom-left panel shows the best-fitting model for MnS obtained by minimizing the χ^2 statistic.

Table 2. Properties of hot Jupiters considered in this study. Eight hot Jupiters from Sing et al. (2016) are shown with predicted atmospheric condensates in the observable atmosphere and the best-fitting slopes to the transmission spectra in the 0.3–0.56 μm range with associated errors. The expected condensates are obtained from Sing et al. (2016)’s fig. 2 between the pressures 10^{-1} and 10^{-3} bar for the planetary-averaged p – T profile. The p – T profile along the terminator can vary from this average by ~ 100 K (see e.g. Morley et al. 2017) but we use these predicted species as fiducial given the overlap in uncertainties in p – T profiles that can be computed from transmission retrieval methods.

Hot Jupiter	Predicted condensates	Best-fitting slope (0.3–0.56 μm)	T_{eq} (K)
WASP-17b	Al_2O_3	-4.25 ± 1.03	1740
WASP-39b	MnS	-3.89 ± 1.28	1120
HD209458b	MgSiO_3 and Mg_2SiO_4	-3.04 ± 0.54	1450
HAT-P-1b	MnS	-4.11 ± 1.73	1320
WASP-31b	MgSiO_3 and Mg_2SiO_4	-5.52 ± 1.27	1580
HAT-P-12b	None	-2.24 ± 2.88	960
HD 189733b	MnS	-7.94 ± 0.61	1200
WASP-6b	MnS	-4.14 ± 1.36	1150

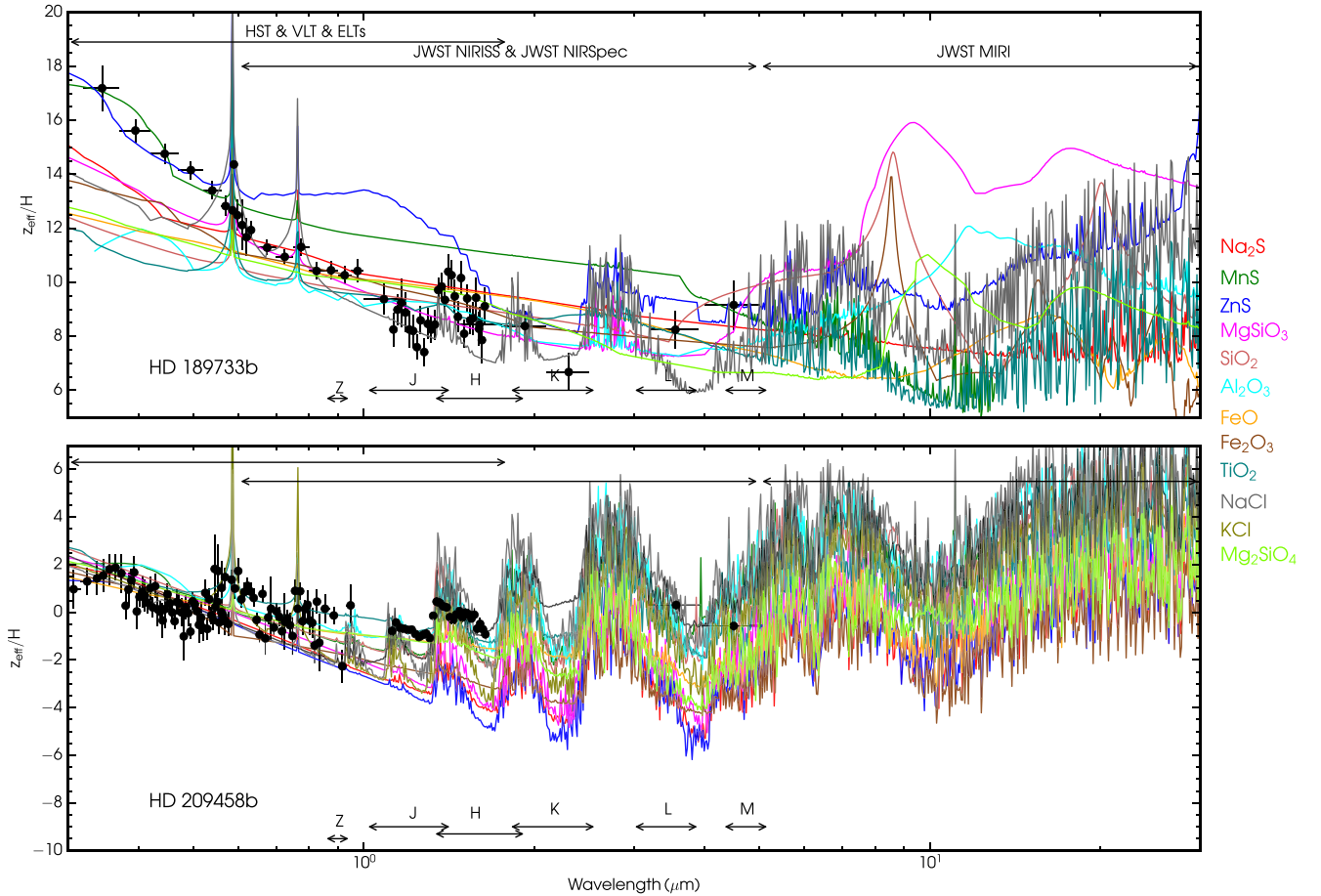


Figure 7. Transmission spectra of HD 189733b and HD 209458b. Each coloured curve represents an H_2 -rich atmosphere with the corresponding condensate as shown in the legend, with additional opacities due to H_2O , $\text{H}_2\text{-H}_2$ and $\text{H}_2\text{-He}$ CIA, and Na and K at solar abundances. The cloud parameters for each coloured curve are chosen to fit the data using the metric of Fig. 2. HD 189733b and HD 209458b coloured models are for $0.01 \times$ solar and supersolar H_2O abundances, respectively. The black curve is a benchmark model with no condensates nor Na and K opacity, but includes $0.01 \times$ solar H_2O , and $\text{H}_2\text{-H}_2$ and $\text{H}_2\text{-He}$ CIA opacity. The black circles show data from Sing et al. (2016).

Madhusudhan (2017) retrieve the same HD 209458b optical spectrum to obtain $\gamma = -15.03^{+4.65}_{-3.36}$, and we determine the optical slope to be $\mathcal{S} = -3.04 \pm 0.54$ (see Table 2). The median cloud scale-height with its 1σ confidence bounds is then $\mathcal{S}/\gamma = H_c/H = 0.20^{+0.14}_{-0.06}$. An H_c value of $0.20H$ suggests that clouds on HD 209458b may indeed be patchy or inhomogeneous. Our one-dimensional cloud model shows that homogeneous clouds cannot be probed in transmission spectra for $H_c/H \lesssim 0.4$ (see Section 3.1). Given a slope \mathcal{S} that is manifestly less steep than -4.2 due to H_2 scattering, one possible corollary is that $H_c/H = 0.20$ suggests an azimuthally averaged value for the day–night terminator, probing inhomogeneous cloud coverage.

The degeneracies and disagreements exposed between our cloud models and present high-precision observations of HD 189733b and HD 209458b call for a detailed approach to cloud modelling in transit spectra. The three key observables using our model are important to interpret cloud properties with high-precision observations using facilities such as *HST*, *JWST*, *VLT* and *ELTs*. Of the three key observable cloud properties, condensate features in the IR show the most immediate promise to cloud characterization given the imminent *JWST* launch. Future IR observations from *JWST* will allow for more detailed studies of clouds with high-precision and high-resolution measurements. Interpretation of the peculiarly steep

slope of HD 189733b and HD 209458b’s optical data will benefit from *JWST*’s broad IR coverage, enabling study of spectra as a whole from 0.6 to $30 \mu\text{m}$.

5 DISCUSSIONS AND CONCLUSIONS

Using models of transmission spectra of cloudy atmospheres, we illustrate three key observables that serve towards constraining detailed cloud properties with high-precision observations. However, detailed characterization of current observations requires more complicated approaches to modelling clouds in transit. There are many rigorous facets of cloud physics that we have not considered, all of which may need incorporation into more sophisticated models in the future.

Condensate particles can form either from direct condensation from supersaturated vapour or by condensing on extant particles of a different composition in processes called homogeneous nucleation and heterogeneous nucleation, respectively. Our model assumes a homogeneous creation of grains, though this assumption may not be the dominant mechanism in some atmospheres (Marley et al. 2013). We have not modelled the formation mechanism of cloud particulates either through homogeneous or heterogeneous nucleation mechanisms because the simplistic picture of all vapour

condensing at saturation ratios above unity is shown to be inaccurate, at least for some combinations of vapours and nucleation seeds. For example, the experiments of Iraci et al. (2010) suggest that water ice condensation on surrogate materials in the Martian atmosphere is more difficult than presumed. They find that saturation ratios of 2.5 or more are needed for cloud formation.

We have assumed homogeneous, isotropic spherical particles in contrast with irregular particles (e.g. ellipsoids, discs and fractals). The spherical assumption is idealized and yet has been of great use in understanding many scattering phenomena. We have not considered scattering from arbitrarily irregular particulates for two reasons. First, the domains of validity of modified Mie theories are not extensively tested and are not self-consistent in all cases (see e.g. Schuerman 1980). For example, Schuerman (1980) explains that the modified theory of Chylek, Grams & Pinnick (1976) violates energy conservation and predicts total extinction cross-sections that are different from the scattering cross-sections for a purely real refractive index (no absorption), an unphysical result. Secondly, even under the assumption of self-coherency and exactness, these modified theories are not of much practical use due to our ignorance on the shapes of particles in exoplanetary atmospheres.

In the present work, we investigate key metrics to characterize clouds in exoplanetary atmospheres using transmission spectra. We construct model spectra to explore three key observables of clouds: the slope in the optical, the uniformity of this slope and features in the IR. We have explored the first observable through the effects of cloud composition, modal particle size and scaleheight on the spectral slope in a clean spectral window in the visible. Secondly, we have studied which condensates produce uniform/non-uniform slopes in the optical that are discernible given the precision of current data sets. These two metrics will be of high utility with observations of high-precision transmission spectra in the optical. The third key observable shows the promise of using IR spectra to further constrain cloud properties.

Our study of cloud optical slopes shows that very steep slopes of $|S| > 5$ suggest the existence of sulphide clouds. Smaller slope values of $|S| < 5$ show degenerate fits for different cloud species and modal particle sizes for fixed cloud scaleheight. Consideration of different scaleheights still shows degenerate fits, in that large modal particle sizes with large scaleheights mimic slopes from smaller particles with smaller scaleheights. Below a scaleheight of $H_c \approx 2H/5$, cloud dominance diminishes and the optical slopes of transmission spectra tend towards the H_2 Rayleigh scattering value of -4.2 in the window $0.3\text{--}0.56\ \mu\text{m}$. Therefore, observable properties of homogeneous clouds are expressed in transmission spectra only for $H_c \gtrsim 2H/5$. Values of H_c smaller than $0.4H$ suggest either inhomogeneous clouds or cloud-free atmospheres dominated by H_2 Rayleigh scattering. Finally, a slope of about -4 does not of itself suggest H_2 Rayleigh scattering since such a slope is produced in the Rayleigh regime for many condensates for large scaleheights (e.g. sulphides and chlorides). One way towards lifting these degenerate fits is through determination of the p - T profile through retrieval methods.

Observed transmission spectra in the optical are usually fitted by straight lines characterized by uniform slopes (e.g. Sing et al. 2016). However, spectra of condensate species do not all show uniform gradients. For example, whilst NaCl and KCl show linear slopes for a modal size of $0.01\ \mu\text{m}$, MnS particulates of the same size distribution show a strong characteristic valley at $\sim 0.5\ \mu\text{m}$ causing significant deviation from linearity. Four of the 12 species considered in this work have significant deviations from uniform optical slopes: MnS, ZnS, Fe_2O_3 and TiO_2 . By corollary, the majority of

considered cloud types possess observationally limited uniform slopes in the Rayleigh regime: Na_2S , Al_2O_3 , FeO , Mg_2SiO_4 , MgSiO_3 , NaCl, KCl, SiO_2 . Future high-precision observations in the optical should be able to lift degeneracies in cloud characterization through these two groups of clouds: those that show substructure in optical slopes and those that are significantly linear. Species can then be further constrained through the first and third observables.

IR signatures of cloud species show a promising avenue for discovering condensates in transit spectra. Observations in the IR have potential to disambiguate degeneracies seen from the optical spectra alone. As against the canonical assumption, we find that IR features can be due to both absorption and scattering of radiation. For example, MnS particles of modal sizes $a_0 > 0.1\ \mu\text{m}$ contribute to extinction at $\sim 4\ \mu\text{m}$ by scattering of incident radiation. The cloud features most amenable for future spectral interpretation are those that appear even with high atmospheric water abundances. There are four cloud types with features most promising for future identification with *JWST*. SiO_2 and Fe_2O_3 have narrow peaks at $\sim 8\text{--}9\ \mu\text{m}$ and Mg_2SiO_4 and MgSiO_3 possess broad peaks at broad peak at $\sim 8\text{--}12\ \mu\text{m}$.

We apply our metrics to current observations of eight hot Jupiters. For six of the planets, the current precisions on the spectra allow for a wide range of solutions, suggesting the need for higher precision spectra. For the planets with the most precise data, HD 209458b and HD 189733b, we find generally degenerate fits to the optical spectrum of HD 209458b with a few marginally favoured solutions, while the spectrum of HD 189733b is challenging to explain by any of the species considered. Overall, our work highlights the importance of broad-band (optical-IR) high-precision transmission spectra as well as detailed theoretical models for reliable inferences of cloud properties in transiting exoplanetary atmospheres. Focused observations with current facilities (e.g. *HST* and VLT) as well as upcoming facilities (e.g. *JWST*, ELTs) promise new advancements in this direction. The three empirical metrics presented in our current work will prove useful in the characterization of clouds in exoplanetary atmospheres using high-precision transmission spectra.

ACKNOWLEDGEMENTS

AP is grateful for research funding from the Gates Cambridge Trust. AP thanks Rik van Lieshout, Ryan MacDonald and Sidharth Gandhi for helpful discussions. We thank the referee for useful comments that have added to the quality of our work. This research has made use of NASA's Astrophysics Data System.

REFERENCES

- Ackerman A. S., Marley M. S., 2001, *ApJ*, 556, 872
 Bean J. L. et al., 2011, *ApJ*, 743, 92
 Benneke B., Seager S., 2012, *ApJ*, 753, 100
 Bétrémieux Y., Swain M. R., 2017, *MNRAS*, 467, 2834
 Bohren C. F., Huffman D. R., 1983, *Absorption and Scattering of Light by Small Particles*. Wiley, New York
 Box M. A., 1983, *Aust. J. Phys.*, 36, 701
 Brooke T. Y., Knacke R. F., Encrenaz T., Drossart P., Crisp D., Feuchtgruber H., 1998, *Icarus*, 136, 1
 Budaj J., Kocifaj M., Salmeron R., Hubeny I., 2015, *MNRAS*, 454, 2
 Burrows A. S., 2014, *Proc. Natl. Acad. Sci.*, 111, 12601
 Burrows A., Sharp C. M., 1999, *ApJ*, 512, 843
 Carlson B. E., Lacin A. A., Rossow W. B., 1994, *J. Geophys. Res.*, 99, 14
 Chylek P., Grams G. W., Pinnick R. G., 1976, *Science*, 193, 480
 de Wit J., Seager S., 2013, *Science*, 342, 1473

Deirmendjian D., 1964, *Appl. Opt.*, 3, 187
 Deirmendjian D., 1969, *Electromagnetic Scattering on Spherical Polydispersions*. Elsevier, New York
 Demory B.-O. et al., 2013, *ApJ*, 776, L25
 Draine B. T., 2006, *ApJ*, 636, 1114
 Draine B. T., Lee H. M., 1984, *ApJ*, 285, 89
 Ehrenreich D. et al., 2014, *A&A*, 570, A89
 Evans T. M. et al., 2016, *ApJ*, 822, L4
 Fortney J. J., 2005, *MNRAS*, 364, 649
 Fortney J. J., Mordasini C., Nettelmann N., Kempton E. M.-R., Greene T. P., Zahnle K., 2013, *ApJ*, 775, 80
 Graaff R., Aarnoudse J. G., Zijp J. R., Sloot P. M. A., de Mul F. F. M., Greve J., Koelink M. H., 1992, *Appl. Opt.*, 31, 1370
 Greene T. P., Line M. R., Montero C., Fortney J. J., Lustig-Yaeger J., Luther K., 2016, *ApJ*, 817, 17
 Helling C., 2008, in Fischer D., Rasio F. A., Thorsett S. E., Wolszczan A., eds, *ASP Conf. Ser. Vol. 398, Extreme Solar Systems*. Astron. Soc. Pac., San Francisco, p. 443
 Helling C., Dehn M., Woitke P., Hauschildt P. H., 2008, *ApJ*, 675, L105
 Helling C. et al., 2016, *MNRAS*, 460, 855
 Heng K., 2016, *ApJ*, 826, L16
 Howe A. R., Burrows A. S., 2012, *ApJ*, 756, 176
 Hubeny I., Burrows A., Sudarsky D., 2003, *ApJ*, 594, 1011
 Iraci L. T., Phebus B. D., Stone B. M., Colaprete A., 2010, *Icarus*, 210, 985
 Knutson H. A., Benneke B., Deming D., Homeier D., 2014a, *Nature*, 505, 66
 Knutson H. A. et al., 2014b, *ApJ*, 794, 155
 Kreidberg L. et al., 2014a, *Nature*, 505, 69
 Kreidberg L. et al., 2014b, *ApJ*, 793, L27
 Lecavelier Des Etangs A., Pont F., Vidal-Madjar A., Sing D., 2008, *A&A*, 481, L83
 Lee G., Dobbs-Dixon I., Helling C., Bognar K., Woitke P., 2016, *A&A*, 594, A48
 Lee J.-M., Irwin P. G. J., Fletcher L. N., Heng K., Barstow J. K., 2014, *ApJ*, 789, 14
 Line M. R., Parmentier V., 2016, *ApJ*, 820, 78
 McCullough P. R., Crouzet N., Deming D., Madhusudhan N., 2014, *ApJ*, 791, 55
 MacDonald R. J., Madhusudhan N., 2017, *MNRAS*, 469, 1979
 Madhusudhan N., Seager S., 2009, *ApJ*, 707, 24
 Madhusudhan N. et al., 2011, *Nature*, 469, 64
 Madhusudhan N., Crouzet N., McCullough P. R., Deming D., Hedges C., 2014, *ApJ*, 791, L9
 Madhusudhan N., Agúndez M., Moses J. I., Hu Y., 2016, *Space Sci. Rev.*, 205, 285
 Marley M. S., Ackerman A. S., Cuzzi J. N., Kitzmann D., 2013, *Clouds and Hazes in Exoplanet Atmospheres*. Univ. Arizona Press, Tucson, p. 367
 Mbarek R., Kempton E. M.-R., 2016, *ApJ*, 827, 121
 Mordasini C., van Boekel R., Mollière P., Henning T., Benneke B., 2016, *ApJ*, 832, 41
 Morley C. V., Fortney J. J., Kempton E. M.-R., Marley M. S., Visscher C., Zahnle K., 2013, *ApJ*, 775, 33
 Morley C. V., Knutson H., Line M., Fortney J. J., Thorngren D., Marley M. S., Teal D., Lupu R., 2017, *AJ*, 153, 86
 Oshagh M., Santos N. C., Ehrenreich D., Haghighipour N., Figueira P., Santerne A., Montalto M., 2014, *A&A*, 568, A99
 Parmentier V., Showman A. P., Lian Y., 2013, *A&A*, 558, A91
 Pont F., Knutson H., Gilliland R. L., Moutou C., Charbonneau D., 2008, *MNRAS*, 385, 109
 Pont F., Sing D. K., Gibson N. P., Aigrain S., Henry G., Husnoo N., 2013, *MNRAS*, 432, 2917
 Sánchez-Lavega A., Pérez-Hoyos S., Hueso R., 2004, *Am. J. Phys.*, 72, 767
 Schuerman D. W., 1980, *Light Scattering by Irregularly Shaped Particles*. Plenum, New York
 Seager S., 2010, *Exoplanet Atmospheres: Physical Processes*. Princeton Univ. Press, Princeton, NJ
 Sharp C. M., Burrows A., 2007, *ApJS*, 168, 140
 Sing D. K. et al., 2016, *Nature*, 529, 59

Stognienko R., Henning T., Ossenkopf V., 1995, *A&A*, 296, 797
 Tazzari M. et al., 2016, *A&A*, 588, A53
 Vahidinia S., Cuzzi J. N., Marley M., Fortney J., 2014, *ApJ*, 789, L11
 Van de Hulst H. C., 2003, *Light Scattering by Small Particles*. Dover Press, New York
 Wakeford H. R., Sing D. K., 2015, *A&A*, 573, A122
 Wakeford H. R., Visscher C., Lewis N. K., Kataria T., Marley M. S., Fortney J. J., Mandell A. M., 2017, *MNRAS*, 464, 4247

APPENDIX A: EFFECTIVE ALTITUDE FORMULATIONS

There is an alternative formulation to equation (1) for the effective altitude in transmission derived through considering how much flux is absorbed in the planetary atmosphere. The differential amount of flux traversing the terminator at a radius r from the planetary centre and received by a distant observer at distance d is

$$d\mathcal{F}_\lambda \Big|_r = \mathcal{I}_{\lambda,r} dA_r = \mathcal{I}_{\lambda,r} 2\pi r dr / d^2 \quad (\text{A1})$$

$$= \mathcal{I}_{\lambda_i} e^{-\tau(\lambda,r)} 2\pi r dr / d^2 \quad (\text{A2})$$

such that the total flux received to the stellar radius (where $\tau \equiv 0$) is thus

$$\mathcal{F}_{\lambda,r} = \int_0^{R_*} d\mathcal{F}_\lambda \Big|_r = \frac{\mathcal{I}_{\lambda_i}}{d^2} \int_0^{R_*} 2\pi r e^{-\tau(\lambda,r)} dr. \quad (\text{A3})$$

The difference between the integrated initial stellar flux and the integrated received fluxes, the total absorbed flux, is then

$$\mathcal{F}_{\lambda,a} = \mathcal{F}_{\lambda_i} - \mathcal{F}_{\lambda,r} = \frac{\mathcal{I}_{\lambda_i}}{d^2} \int_0^{R_*} 2\pi r dr - \frac{\mathcal{I}_{\lambda_i}}{d^2} \int_0^{R_*} e^{-\tau(\lambda,r)} 2\pi r dr \quad (\text{A4})$$

$$\mathcal{I}_{\lambda_i} \pi R_{p,\lambda}^2 = \mathcal{I}_{\lambda_i} \int_0^{R_*} (1 - e^{-\tau(\lambda,r)}) 2\pi r dr. \quad (\text{A5})$$

Each planetary annulus is weighted by its corresponding absorbance $1 - e^{-\tau(\lambda,r)}$ from the planetary centre outwards,

$$\pi R_{p,\lambda}^2(\lambda) = \pi [R_{p0} + z_{\text{eff}}(\lambda)]^2, \quad (\text{A6})$$

$$= \int_0^{R_*} 2\pi r (1 - e^{-\tau(\lambda,r)}) dr, \quad (\text{A7})$$

where R_{p0} is the radius of the planet for which the atmosphere becomes optically thick to all wavelengths. This formulation is equivalent to that of de Wit & Seager (2013). Equations (A6) and (A7) readily become

$$2R_{p0} z_{\text{eff}}(\lambda) + z_{\text{eff}}^2(\lambda) = \int_{R_{p0}}^{R_*} 2r (1 - e^{-\tau(\lambda,r)}) dr. \quad (\text{A8})$$

This is a quadratic equation for $z_{\text{eff}}(\lambda)$ whose solution – with the substitution that $z = r - R_{p0}$ in the integral – gives the final form for the effective altitude,

$$z_{\text{eff}}(\lambda) = R_{p0} (\sqrt{1 + \aleph_0} - 1), \quad (\text{A9})$$

where

$$\aleph_0 \equiv \int_0^{R_* - R_{p0}} \frac{2}{R_{p0}} \left(\frac{z}{R_{p0}} + 1 \right) (1 - e^{-\tau(\lambda,z)}) dz. \quad (\text{A10})$$

As the optical depth $\tau(\lambda, z)$ appears in the exponent and z is always ≥ 0 , $z_{\text{eff}} \geq 0$ and $R_p(\lambda) \geq R_{p0}$. Therefore, in this model R_{p0} acts as a hard surface, whereas in our model it is a reference radius for which z_{eff} can lie either below or above.

The instantaneous slope of this effective altitude at any λ from equation (A9) is

$$\frac{d(z_{\text{eff}}/H)}{d \ln \lambda} = \gamma \frac{\int_0^{R_* - R_{p0}} (z/R_{p0} + 1) e^{-\tau} \tau dz}{H(1 + \kappa_0)^{1/2}} \equiv \gamma \eta, \quad (\text{A11})$$

where γ is the power on the effective extinction cross-section, $\sigma' = \sigma_0(a)(\lambda/\lambda_0)^{\gamma(a, \lambda)}$. This is essentially the equivalent expression to equation (3). In the non-Rayleigh limit, η equals to H_c/H but for small size parameters (or the Rayleigh limit) these two relations are not equal.⁴ Our numerical formulation of the effective altitude and those of Lecavelier Des Etangs et al. (2008) and Wakeford & Sing (2015) use R_{p0} as a reference altitude for which a negative effective altitude is allowed. This different formulation equivalent to that of de Wit & Seager (2013) is by construction such that R_{p0} is a hard planetary surface for which the effective altitude can only lie above or at the surface. B  tr  mieux & Swain (2017) treat Lecavelier Des Etangs et al. (2008) and de Wit & Seager (2013)'s prescriptions as similar in trying to develop a formalism for the effective altitude that accounts for a hard planetary surface. They are mistaken in both considering the two formulations as similar and moreover in claiming that the model of de Wit & Seager (2013) has no hard 'surface'. In fact, as the slant optical depth decreases at the surface (e.g. by considering smaller particles dominating the extinction), de Wit & Seager (2013)'s model *does* asymptotically approach the planetary surface without going below, unlike our formulation. B  tr  mieux & Swain (2017)'s equation 33 is therefore precisely the same as de Wit & Seager (2013)'s; when their $\tau_s \rightarrow 0$, the $\eta \rightarrow 0$ such that the logarithmic slope in equation (A11) tends to zero, whilst when their τ_s tends to large values, the $\eta \rightarrow H_c/H$ such that the logarithmic slope tends to $\gamma H_c/H$.

APPENDIX B: COMPUTING MIE COEFFICIENTS

We have carried out an extensive study of the Deirmendjian (1969) form for computing the Mie coefficients a_n and b_n . The values for these coefficients are Deirmendjian (1969)

$$a_n(m, x) = \{\Theta_1 J_{n+1/2}(x) - J_{n-1/2}(x)\} \times \{\Theta_1 [J_{n+1/2}(x) + i(-1)^n J_{-n-1/2}(x)] - [J_{n-1/2} - i(-1)^n \times J_{-n+1/2}(x)]\}^{-1} \quad (\text{B1})$$

$$b_n(m, x) = \{\Theta_2 J_{n+1/2}(x) - J_{n-1/2}(x)\} \times \{\Theta_2 [J_{n+1/2}(x) + i(-1)^n J_{-n-1/2}(x)] - [J_{n-1/2} - i(-1)^n \times J_{-n+1/2}(x)]\}^{-1}. \quad (\text{B2})$$

These coefficients are nearly identical except for the differences in Θ_1 and Θ_2 , which are $\Theta_1 = A_n(mx)/m + n/x$ and $\Theta_2 = mA_n(mx) + n/x$, with $A_n(mx) = J_{n-1/2}(mx)/J_{n+1/2}(mx) - n/(mx)$.⁵

However, we find that these coefficients are not in forms best suited for computations [see also discussion on page 127 of Bohren

& Huffman (1983)]. For some small volumes of parameter space $\{a, \lambda, n(\lambda), \kappa(\lambda)\}$, the expressions of the Deirmendjian (1969) formulation break down giving 'NaN's. This principally occurs for large parameter sizes x . As Section 2.2 notes, an increased x translates into greater numbers of terms in the sum of the scattering and extinction coefficients. The numerical round-off error associated with finite representation of the irrationally valued Bessel functions accumulates such that 'NaN's arise in evaluations for large number of summation terms. Our Mie theory code therefore follows Bohren & Huffman (1983) in computing these two coefficients,

$$a_n(m, x) = \frac{\{D_n(mx)/m + n/x\} \psi_n(x) - \psi_{n-1}(x)}{\{D_n(mx)/m + n/x\} \xi_n(x) - \xi_{n-1}(x)}, \quad (\text{B3})$$

$$b_n(m, x) = \frac{\{m D_n(mx) + n/x\} \psi_n(x) - \psi_{n-1}(x)}{\{m D_n(mx) + n/x\} \xi_n(x) - \xi_{n-1}(x)}, \quad (\text{B4})$$

where $D_n = (\ln \psi_n)'$ and satisfies the backward recurrence relation $D_{n-1} = m/(mx) - (D_n + n/(mx))^{-1}$. This recurrence relation is stable when computed from the maximal value of the series n_{max} downwards. Further, the Riccati–Bessel functions, ψ_n and ξ_n , are

$$\psi_n(z) = \sqrt{\frac{\pi z}{2}} J_{n+1/2}(z) \quad (\text{B5})$$

$$\xi_n(z) = \sqrt{\frac{\pi z}{2}} \{J_{n+1/2}(z) - i Y_{n+1/2}(z)\} = \psi_n(z) - i \chi_n(z), \quad (\text{B6})$$

where $J_{n+1/2}$ and $Y_{n+1/2}$ are the Bessel functions of first and second kind with fractional orders. The Riccati–Bessel functions satisfy the following recurrence relations computed in ascending fashion

$$\psi_{n+1}(x) = \frac{2n+1}{x} \psi_n(x) - \psi_{n-1}(x) \quad (\text{B7})$$

$$\xi_{n+1}(x) = \frac{2n+1}{x} \xi_n(x) - \xi_{n-1}(x) \quad (\text{B8})$$

with initial values of

$$\begin{aligned} \psi_{-1} &= \cos x & \chi_{-1} &= -\sin x \\ \psi_0 &= \sin x & \chi_0 &= \cos x. \end{aligned} \quad (\text{B9})$$

APPENDIX C: GRAIN ABUNDANCE

We here outline the assumptions that go in to the calculation of the condensate grain abundance for a grain composed of a single species. The grain abundance for grains of fixed size assuming a dominant H_2 background is

$$\xi_{\text{grain}} = \frac{\text{Number of grains per volume}}{\text{Number of } H_2 \text{ per volume}} = \frac{n_{\text{grain}}}{n_{H_2}}. \quad (\text{C1})$$

The number of grains in unit volume is

$$n_{\text{grain}} = \frac{\text{Number of dominant atom type per volume}}{\text{Number of dominant atom type per grain}} = \frac{n_d}{N_d}. \quad (\text{C2})$$

Assuming that H_2 dominates the number of atoms per unit volume, the number density of the dominant atom type reads

$$n_d = \xi_d \times \text{Number of atoms per unit volume} = \xi_d \times 2n_{H_2}. \quad (\text{C3})$$

⁴ The Rayleigh limit relations for the absorption and scattering cross-sections are formally applicable in the condition $|m(\lambda)|x \ll 1$ rather than the oft-cited $x \ll 1$.

⁵ The relations for a_n and b_n in Sharp & Burrows (2007) are slightly wrong. We have carried out thorough comparisons of our Mie theory code with the classic work of Deirmendjian (1969) that reveal this. Equations 33 and 34 in Sharp & Burrows (2007) should have second multiplicative terms with exponents of '−1' instead of the current '1'.

As each grain is pure, we are enabled to write

$$N_d = \text{Number of condensate species per grain} = \frac{M_{\text{grain}}}{\mu_{\text{cond}}}. \quad (\text{C4})$$

With these assumptions, the volumetric number density of the grains is

$$n_{\text{grain}} = \frac{2n_{\text{H}_2}\mu_{\text{cond}}\xi_d}{M_{\text{grain}}}. \quad (\text{C5})$$

A spherical grain implies $M_{\text{grain}} = 4\pi a^3 \rho_{\text{grain}}/3$ and therefore the averaged grain abundance is

$$\xi_{\text{grain}} = \frac{3\xi_d\mu_{\text{cond}}}{2\rho_{\text{grain}}\pi a^3}. \quad (\text{C6})$$

This paper has been typeset from a $\text{\TeX}/\text{\LaTeX}$ file prepared by the author.